The CLAS12 Spectrometer at Jefferson Laboratory

V.D. Burkert [40,*], L. Elouadrhiri [40], K.P. Adhikari [28], S. Adhikari [12], M.J. Amaryan [33],
D. Anderson [40], G. Angelini [13], M. Antonioli [40], H. Atac [39], S. Aune [4], H. Avakian [40],
C. Ayerbe Gayoso [47,28], N. Baltzell [40], L. Barion [15], M. Battaglieri [17,40], V. Baturin [40],
I. Bedlinskiy [29], F. Benmokhtar [8], A. Bianconi [43,20], A.S. Biselli [10], P. Bonneau [40], F. Bossù [4],
S. Boyarinov [40], W.J. Briscoe [13], W.K. Brooks [41], K. Bruhwel [40], D.S. Carman [40], A. Celentano [17],
G. Charles [21,33], P. Chatagnon [21], T. Chetry [28,32], G. Christiaens [44,4], S. Christo [40], G. Ciullo [15,11],
B.A. Clary [6], P.L. Cole [25,14], M. Contalbrigo [15], M. Cook [40], V. Crede [27], R. Cruz-Torres [26],
C. Cuevas [40], A. D'Angelo [18,36], N. Dashyan [48], M. Defurne [4], A. Deur [40], R. De Vita [17], S. Diehl [6],
C. Djalali [32,38], G. Dodge [33], R. Dupre [21], M. Ehrhart [1,21], L. El Fassi [28], B. Eng [40], T. Ewing [40],
R. Fair [40], G. Fedotov [32], A. Filippi [19], T.A. Forest [14], M. Garçon [4], G. Gavalian [40], P. Ghoshal [40],
G.P. Gilfoyle [35], K. Giovanetti [23], F.X. Girod [40], D.I. Glazier [44], E. Golovatch [37], R.W. Gothe [38],
Y. Gotra [40], K.A. Griffioen [47], M. Guidal [21], V. Gyurjyan [40], K. Hafidi [1], H. Hakobyan [41,48],
C. Hanretty [40], N. Harrison [40], M. Hattawy [33,1], F. Hauenstein [33], T.B. Hayward [47], D. Heddle [5,40],
P. Hemler [40], O.A. Hen [26], K. Hicks [32], A. Hobart [21], J. Hogan [40], M. Holtrop [30], Y. Ilieva [38],
I. Illari [13], D. Insley [40], D.G. Ireland [44], B.S. Ishkhanov [37], E.L. Isupov [37], G. Jacobs [40], H.S. Jo [24],
R. Johnston [26], K. Joo [6], T. Kageya [40], D. Kashy [40], C. Keith [40], D. Keller [46],
M. Khachatryan [33], A. Khanal [12], A. Kim [6], C.W. Kim [13], W. Kim [24], V. Kubarovsky [40], S.E. Kuhn [33],
L. Lanza [18], M. Leffel [40], V. Lucherini [16], A. Lung [40], M.L. Kabir [28], M. Leali [43,20], S. Lee [26],
P. Lenisa [15], K. Livingston [44], M. Lowry [40], I.J.D. MacGregor [44], I. Mandjavidze [4], D. Marchand [21],
N. Markov [6], V. Mascagna [42,20,43], B. McKinnon [44], M. McMullen [40], C. Mealer [40], M.D. Mestayer [40],
Z.E. Meziani [1,39], R. Miller [40], R.G. Milner [26], T. Mineeva [41], M. Mirazita [16], V. Mokeev [40],
P. Moran [26], A. Movsisyan [15], C. Munoz Camacho [21], P. Naidoo [44], S. Nanda [28], J. Newton [33],
S. Niccolai [21], G. Niculescu [23], M. Osipenko [17], M. Paolone [39], L.L. Pappalardo [15],
R. Paremuzyan [30], O. Pastor [40], E. Pasyuk [40], W. Phelps [5,13], O. Pogorelko [29], J. Poudel [33],
J.W. Price [2], K. Price [21], S. Procureur [4], Y. Prok [33], D. Protopopescu [44], R. Rajput-Ghoshal [40],
B.A. Raue [12,40], B. Raydo [40], M. Ripani [17], J. Ritman [22], A. Rizzo [18,36], G. Rosner [44], P. Rossi [40],
J. Rowley [32], B.J. Roy [22], F. Sabatié [4], C. Salgado [31], S. Schadmand [22], A. Schmidt [26,13],
E.P. Segarra [26], V. Sergeyeva [21], Y.G. Sharabian [40], U. Shrestha [32], Iu. Skorodumina [38,37],
G.D. Smith [9], L.C. Smith [46,40], D. Sokhan [44], O. Soto [16,41], N.Sparveris [39], S. Stepanyan [40],
P. Stoler [34], S. Strauch [38], J.A. Tan [24], M. Taylor [40], D. Tilles [40], M. Turisini [16], N. Tyler [38],
M. Ungaro [40], L. Venturelli [43,20], H. Voskanyan [48], E. Voutier [21], D. Watts [45], X. Wei [40],
L.B. Weinstein [33], C. Wiggins [40], M. Wiseman [40], M.H. Wood [3], A. Yegneswaran [40], G. Young [40],
N. Zachariou [45], M. Zarecky [40], J. Zhang [46], Z.W. Zhao [7,33], V. Ziegler [40]

[1] *Argonne National Laboratory, Argonne, IL 60439, United States of America*
[2] *California State University, Dominguez Hills, Carson, CA 90747, United States of America*
[3] *Canisius College, Buffalo, NY 14208, United States of America*
[4] *IRFU, CEA, Université Paris-Saclay, F-91191 Gif-sur-Yvette, France*
[5] *Christopher Newport University, Newport News, VA 23606, United States of America*

* Corresponding author.
  E-mail addresses: dr.v.burkert@gmail.com, burkert@jlab.org (V.D. Burkert).

[6] *University of Connecticut, Storrs, CT 06269, United States of America*
[7] *Duke University, Durham, NC 27708, United States of America*
[8] *Duquesne University, Pittsburgh, PA 15282, United States of America*
[9] *Edinburgh University, Edinburgh EH9 3JZ, United Kingdom*
[10] *Fairfield University, Fairfield, CT 06824, United States of America*
[11] *Universita' di Ferrara, 44121 Ferrara, Italy*
[12] *Florida International University, Miami, FL 33199, United States of America*
[13] *The George Washington University, Washington, DC 20052, United States of America*
[14] *Idaho State University, Pocatello, ID 83209, United States of America*
[15] *INFN, Sezione di Ferrara, 44100 Ferrara, Italy*
[16] *INFN, Laboratori Nazionali di Frascati, 00044 Frascati, Italy*
[17] *INFN, Sezione di Genova, 16146 Genova, Italy*
[18] *INFN, Sezione di Roma Tor Vergata, 00133 Rome, Italy*
[19] *INFN, Sezione di Torino, 10125 Torino, Italy*
[20] *INFN, Sezione di Pavia, 27100 Pavia, Italy*
[21] *Institut de Physique Nucléaire, IN2P3-CNRS, Université Paris-Sud, Université Paris-Sacla, F-91406 Orsay, France*
[22] *Institute fur Kernphysik (Juelich), 52428 Juelich, Germany*
[23] *James Madison University, Harrisonburg, VA 22807, United States of America*
[24] *Kyungpook National University, Daegu 41566, Republic of Korea*
[25] *Lamar University, Beaumont, TX 77710, United States of America*
[26] *Massachusetts Institute of Technology, Cambridge, MA 02139, United States of America*
[27] *Florida State University, Tallahassee, FL 32306, United States of America*
[28] *Mississippi State University, Mississippi State, MS, 39762, United States of America*
[29] *National Research Centre Kurchatov Institute - ITEP, Moscow, 117259, Russia*
[30] *University of New Hampshire, Durham, NH 03824, United States of America*
[31] *Norfolk State University, Norfolk, VA 23504, United States of America*
[32] *Ohio University, Athens, OH 45701, United States of America*
[33] *Old Dominion University, Norfolk, VA 23529, United States of America*
[34] *Rensselaer Polytechnic Institute, Troy, NY 12180, United States of America*
[35] *University of Richmond, Richmond, VA 23173, United States of America*
[36] *Universita' di Roma Tor Vergata, 00133 Rome, Italy*
[37] *Skobeltsyn Institute of Nuclear Physics, Lomonosov Moscow State University, 119234 Moscow, Russia*
[38] *University of South Carolina, Columbia, SC 29208, United States of America*
[39] *Temple University, Philadelphia, PA 19122, United States of America*
[40] *Thomas Jefferson National Accelerator Facility, Newport News, VA 23606, United States of America*
[41] *Universidad Técnica Federico Santa María, Casilla 110-V Valparaíso, Chile*
[42] *Universita degli Studi dellInsubria, 22100 Como, Italy*
[43] *Universit'a degli Studi di Brescia, 25123 Brescia, Italy*
[44] *University of Glasgow, Glasgow G12 8QQ, United Kingdom*
[45] *University of York, York YO10 5DD, United Kingdom*
[46] *University of Virginia, Charlottesville, VA 22901, United States of America*
[47] *College of William and Mary, Williamsburg, VA 23187, United States of America*
[48] *Yerevan Physics Institute, 375036 Yerevan, Armenia*

ARTICLE INFO

ABSTRACT

The CEBAF Large Acceptance Spectrometer for operation at 12 GeV beam energy (CLAS12) in Hall B at Jefferson Laboratory is used to study electro-induced nuclear and hadronic reactions. This spectrometer provides efficient detection of charged and neutral particles over a large fraction of the full solid angle. CLAS12 has been part of the energy-doubling project of Jefferson Lab's Continuous Electron Beam Accelerator Facility, funded by the United States Department of Energy. An international collaboration of 48 institutions contributed to the design and construction of detector hardware, developed the software packages for the simulation of complex event patterns, and commissioned the detector systems. CLAS12 is based on a dual-magnet system with a superconducting torus magnet that provides a largely azimuthal field distribution that covers the forward polar angle range up to 35°, and a solenoid magnet and detector covering the polar angles from 35° to 125° with full azimuthal coverage. Trajectory reconstruction in the forward direction using drift chambers and in the central direction using a vertex tracker results in momentum resolutions of <1% and <3%, respectively. Cherenkov counters, time-of-flight scintillators, and electromagnetic calorimeters provide good particle identification. Fast triggering and high data-acquisition rates allow operation at a luminosity of 10^{35} cm^{-2}s^{-1}. These capabilities are being used in a broad program to study the structure and interactions of nucleons, nuclei, and mesons, using polarized and unpolarized electron beams and targets for beam energies up to 11 GeV. This paper gives a general description of the design, construction, and performance of CLAS12.

1. Introduction

Electron scattering has proven an effective way of probing the size and internal structure of subatomic particles such as protons, neutrons, and nuclei. Exploiting energetic electron beams led to rapid progress in our understanding of the internal composition of particles. The extended size of the proton was first mapped out in the mid-1950's [1], and the internal quark substructure was discovered in the late 1960's [2]. Using spin-polarized electrons and spin-polarized targets, the internal quark helicity momentum distribution was mapped out in the 1980's and the following decades, and is still an important research topic today [3]. These experiments required only inclusive measurements, where only the beam particle, electrons or muons, that scattered off the target were detected and kinematically analyzed.

In the decades following these discoveries, it was realized that a more detailed understanding of the internal structure of nucleons requires the reconstruction of fully exclusive or semi-inclusive processes, and hence the detection and kinematical reconstruction of additional mesons and baryons in the final state was required. Other constraints
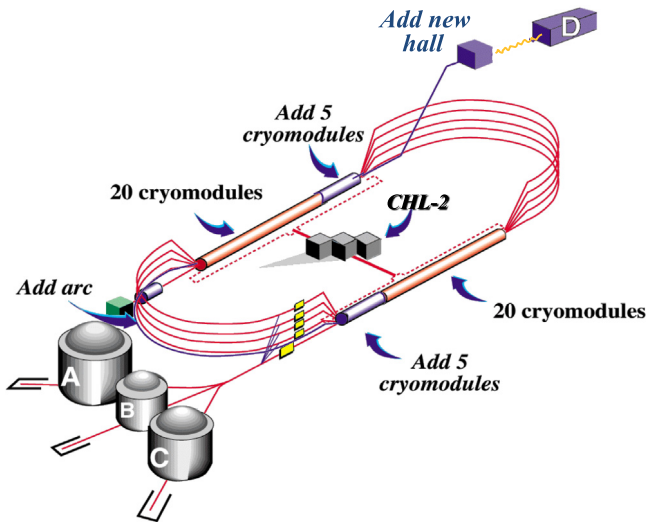
Fig. 1. The CEBAF continuous electron beam accelerator after the doubling of the beam energy to 12 GeV and adding Hall D as a new experimental end station for photon physics experiments. The accelerator is 1400 m in circumference.

came from the need of baryon spectroscopy to measure complete angular distributions, which made it necessary to employ large acceptance devices to serve that purpose. The Continuous Electron Beam Accelerator Facility (CEBAF) [4], the CLAS detector [5], and other experimental equipment at Jefferson Laboratory (JLab) were designed and constructed in the 1990's with these goals in mind and were operated successfully for over 15 years.

The further development of Quantum Chromodynamics (QCD) as the theory of the interaction of colored quarks and gluons, combined with the discovery of the Generalized Parton Distributions (GPDs), provided a novel way that allowed describing the nucleon structure in 3 dimensions (3D), 2 in coordinate space and 1 in momentum space.

The discovery opened up a new avenue of hadronic research that has become one of the flagship programs in nuclear and hadronic physics. The GPDs must be probed in exclusive processes, with deeply virtual Compton scattering being the most suitable one. This is a rather rare process and measurements require the operation of large acceptance detectors at high instantaneous luminosities of 10^{35} cm^{-2}s^{-1} to map out the process in the full kinematic phase space using polarized beams, polarized targets, and sufficiently high beam energy. The complementary process of semi-inclusive deep inelastic scattering (SIDIS) is also of topical interest to probe the internal structure of the nucleon in 3D momentum space. The science program of CLAS12 is very broad [6] and encompasses the study of the structure of the proton and neutron both in their ground state, as well as their many excited states, and in the deeply inelastic kinematics. Other experiments are designed to probe the short range structure of nuclei through measurements of the transparency of nuclei to mesons and baryons, and how it changes with the momentum transfer.

2. The JLab facility at 12 GeV

The CLAS12 detector was designed to study electro-induced nuclear and hadronic reactions by providing efficient detection of charged and neutral particles over a large fraction of the full solid angle. It is based on a combination of a six-coil torus magnet and a high-field solenoid magnet. The combined magnetic field provides a large coverage in both azimuthal and polar angles. Trajectory reconstruction using drift chambers at forward angles results in an average momentum resolution of $\sigma_p/p \approx 0.7\%$ with significant variations over the full polar angle range. At large polar angles, where particle momenta are typically below 1 GeV, the average momentum resolution is $\sigma_p/p \approx 3\%$. Cherenkov counters, time-of-flight systems, and calorimeters provide good particle identification for electrons, charged pions, kaons, and protons. Fast triggering and high data acquisition rates allow operation at luminosities of 10^{35} cm^{-2}s^{-1} for extended periods of time. These capabilities are being used in a broad scientific program to study the structure and interactions of baryons, mesons, and nuclei using polarized and unpolarized targets.
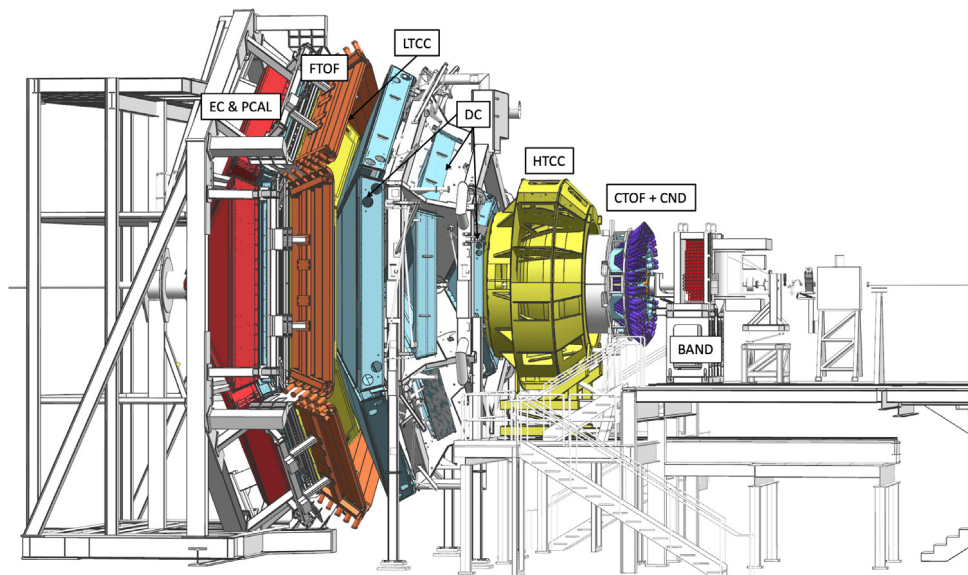

Fig. 2. The CLAS12 detector in the Hall B beamline. The electron beam enters from the right and impinges on the production target located in the center of the solenoid magnet shown at the right (upstream) end of CLAS12, where other detector components are also visible. Scattered electrons and forward-going particles are detected in the Forward Detector (FD) consisting of the High Threshold Cherenkov Counter (HTCC) (yellow) with full coverage in polar angle $5° \le \theta \le 35°$ and $\Delta\phi = 2\pi$ coverage in azimuth. The HTCC is followed by the torus magnet (gray), the drift chamber tracking system (light blue), another set of Cherenkov counters (hidden), time-of-flight scintillation counters (brown), and electromagnetic calorimeters (red). Between the HTCC and the torus, the Forward Tagger is installed to detect electrons and photons at polar angles $2° \le \theta \le 5°$. The Central Detector (CD) consists of the Silicon Vertex Tracker (hidden), which is surrounded by a Barrel Micromesh Tracker (hidden), the Central Time-of-Flight system, and the Central Neutron Detector (PMTs in blue). At the upstream end, a Back Angle Neutron Detector (red) is installed. In the operational configuration. the entire CLAS12 detector extends for 13 m along the beamline. (For interpretation of the references to color in this figure legend, the reader is referred to the web version of this article.)
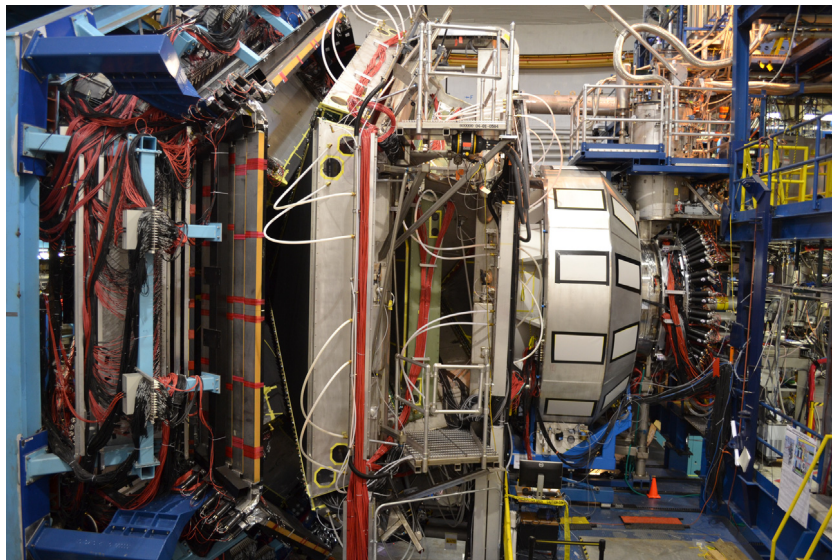
Fig. 3. The CLAS12 detector in the Hall B beamline. The beam enters from the right near the upstream end of the solenoid magnet and the cryogenic service tower, followed by the HTCC and the torus magnet with the drift chambers. The Low Threshold Cherenkov Counter, Forward Time-of-Flight, and the electromagnetic calorimeters (PCAL and EC) are seen at the downstream end to the left.

Fig. 4. The CLAS12 magnet systems. Left: The fully assembled solenoid magnet including all cryogenic connections on the beamline at the beginning of cool down, before the detector installation. Right: The torus magnet with all six coils mechanically assembled in a common cryostat. The coil cryostat, which is fabricated from non-magnetic steel, has an outside width of 124 mm. The cross bars provide a cold (4.5 K) cryogenic connection of neighboring coils, and counteract the out-of-plane forces to provide mechanical stability to the full magnet. Due to the large physical size of the assembled torus magnet, the final assembly of the magnet had to be completed in Hall B.

This paper provides a general description of the design, construction, and performance of CLAS12 and how it expands upon the capabilities provided by the JLab 12 GeV energy upgrade. The CEBAF accelerator and experimental halls are shown for the energy upgraded configuration in Fig. 1. CEBAF is designed from two parallel linear accelerators (linacs) based on superconducting radio frequency (RF) technology, and arranged in a race-track configuration [4]. Spin-polarized electrons are generated in the gun, pre-accelerated in the injector, and subsequently injected and accelerated in the north linac. They are then bent in a 180° arc and injected into the south linac. This is repeated four and a half more times to reach the final energy for Hall D and up to four times for the desired delivery energies to Halls A, B, and C. In the recirculating arcs, electrons are transported in

5 independent out-of-phase tracks of different energies. For 12 GeV operation, five accelerating cryomodules with four times higher gradients than were used in the 6 GeV CEBAF machine were added to each of the two existing linacs to reach a maximum energy of 11 GeV for Halls A, B, and C. One added arc path and one more pass through the north linac were added to achieve the highest beam energy of 12 GeV for Hall D. This highest beam energy is generated exclusively for Hall D, while the other three halls may receive beams at the same beam energy or at different beam energies simultaneously, with up to a factor of 10^5 differences in current from 1 nA to 100 μA.

Major new detectors and other experimental equipment have been installed in Halls B, C, and D that support a broad science program addressing fundamental issues in nuclear and hadronic physics. In Hall D,
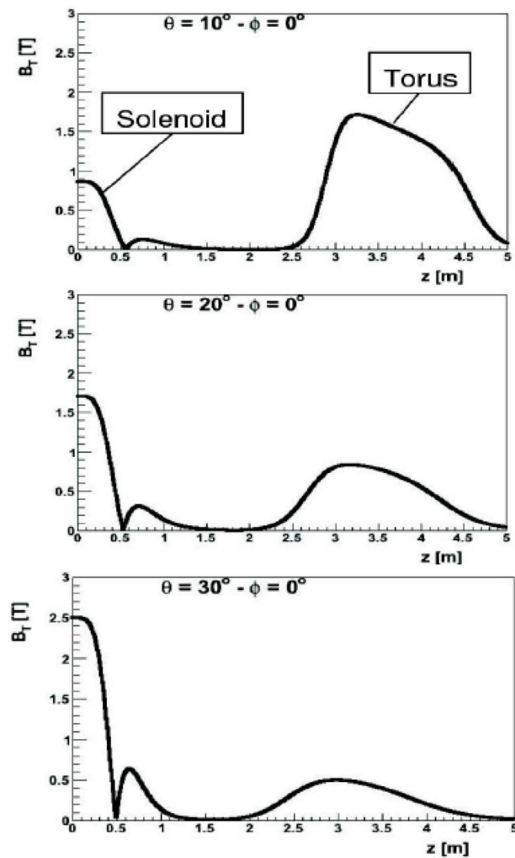
Fig. 5. Combined solenoid and torus magnetic fields, showing the magnetic field component perpendicular to the radial distance from the solenoid center. Only the transverse components act on the charged tracks. At small polar angles the particle deflecting component is small in the solenoid field, while it is largest in the torus magnet. For large polar angle the transverse component is large in the solenoid field and small in the torus field volume.

a large hermetic detector with a solenoid magnet at its core has been in operation since 2015. It incorporates tracking capabilities and photon detection over nearly the full 4π solid angle. This hall is dedicated to the production of mesons employing a linearly polarized photon beam. The new CLAS12 spectrometer, displayed in a side view in Fig. 2 (from the design model) and in Fig. 3 (photograph), features large solid angle coverage and instantaneous luminosities of 10^{35} cm^{-2}s^{-1} for electron scattering experiments with multiple particle final states.

Hall C includes the new super-high momentum magnetic spectrometer (SHMS) in addition to the existing high momentum spectrometer. In Hall A, a new super big bite spectrometer (SBS) has been added to the existing high resolution spectrometer pair HRS[2], and other large installation experiments have been proposed. Complementing the new equipment is the highly spin-polarized electron gun, high-power cryogenic targets, and several spin-polarized targets using NH_3, ND_3, HD, ^{3}He, and ^{7}Li as target materials to support a broad range of polarization measurements.

3. The CLAS12 superconducting magnets

The design of CLAS12 is based on a combination of a toroidal magnetic field at polar angles up to $\approx 35°$ and a 5 T solenoidal field in the central region in the approximate polar angle range $35° \leq \theta \leq 125°$. The primary requirement driving this choice is the ability to measure charged particles at high momentum with good resolution at forward angles, while operating the detector systems at high luminosity. This requires effective shielding of the detector system from
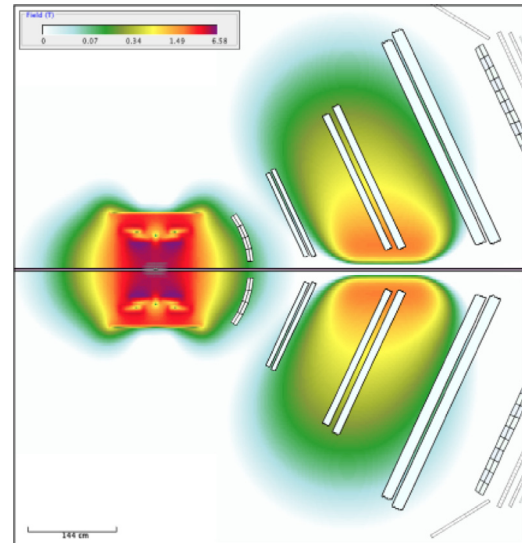

Fig. 6. Combined solenoid and torus magnetic fields. The color code shows the total magnetic field of both the solenoid and torus at full current. The open boxes indicate the locations and dimensions of the active detector elements. (For interpretation of the references to color in this figure legend, the reader is referred to the web version of this article.)

low-energy electrons produced in the target material due to Møller scattering $e^- + e^- \rightarrow e^- + e^-$ of the high-energy beam electrons on atomic electrons in the target material. The large majority of those electrons are prevented from reaching the sensitive detectors as they curl up in the strong longitudinal magnetic field, and are then guided into a shielding pipe made from bulk tungsten material where they dump their energy. The fully assembled torus and solenoid magnets are shown in Fig. 4.

The distribution of the absolute magnetic field along lines of constant polar angle seen from the target position is shown in Fig. 5. Both the torus and solenoid magnetic fields are included. The field distributions of the solenoid and torus magnets are shown in Fig. 6.

3.1. The torus magnet

A contour of one of the six identical coils of the torus magnet is shown in Fig. 7. The geometrical coverage as seen from the target ranges from 5° to 40° in polar angle. The symmetrically arranged six magnet coils provide an approximate toroidal magnetic field around the beamline. The six coils are mounted in a central cold hub on a common stainless-steel cylinder, which also provides the geometrical symmetry for the alignment of the coils near the magnet center (see Fig. 8). This increases placement accuracy of the coil packages in areas where the magnetic field is expected to be maximal. A full view of the assembled torus coils and cryostat is shown in Fig. 4(right). The open range in azimuthal angle depends on the polar angle of the particle trajectory, and ranges from 50% of 2π at 5° to about 90% of 2π at 40°.

Each superconducting coil is made from a two-coil "double-pancake" potted in an aluminum case. The number of windings per pancake is 117. The conductor is Superconducting Super Collider outer dipole cable soldered into a 20 mm × 2.5 mm copper channel with a turn-to-turn insulation of 75 μm fiberglass tape. Operating at a nominal current of 3770 A, the peak field is 3.58 T at the inner turns close to the warm bore. For symmetry reasons the field on the beam axis is ideally equal to zero, with a small remnant field present due to imperfections in the magnet assembly and coil positions. The $\int B dl$ at the nominal current is 2.78 Tm at 5° and 0.54 Tm at 40°. The inductance of the
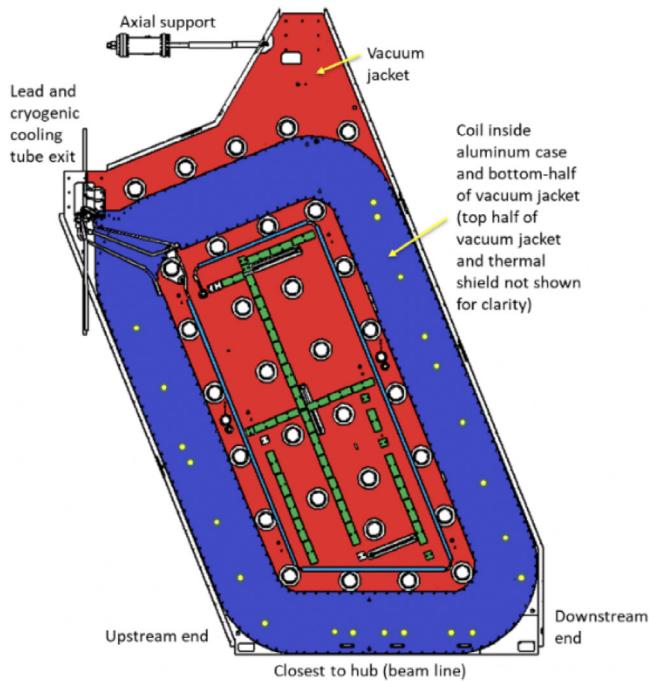
Fig. 7. A torus magnet coil (blue) in its vacuum jacket. All six coils are nominally identical to each other, and are tilted forward at a 22° angle relative to the vertical, and are symmetrically arranged in azimuth. The thickness of the coil package is 0.3 m and the entire coil spans about 2 m × 4 m. (For interpretation of the references to color in this figure legend, the reader is referred to the web version of this article.)
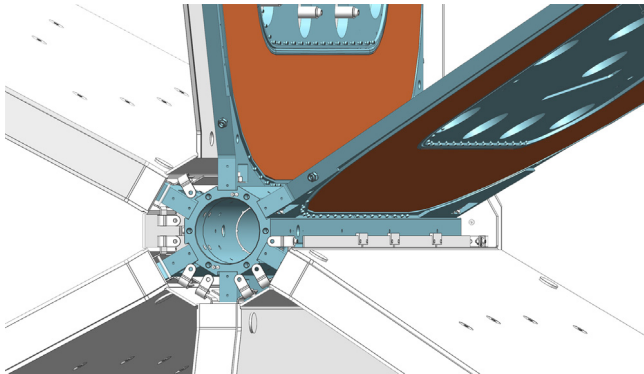
Fig. 8. The six torus coils are mounted on the cold central stainless-steel hub that bears the centripetal force. The dark-shaded areas indicate the location of the superconducting coils, surrounded by the cryostat and vacuum jacket.

magnet is 2.0 H and the stored energy 14.2 MJ. The magnet has liquid-N_2 cooled heat shields. After assembly and cool down, the magnet reached full field immediately. For details on the design and operation of the torus magnet, see Ref. [7].

3.2. The solenoid magnet

The solenoid magnet is a self-shielded superconducting magnet around the beamline used to generate a field primarily in the beam direction. Fig. 9 shows the design layout of the solenoid coils, and the fully assembled magnet is shown in Fig. 4(left). The design is driven by the physics requirements to (a) provide a magnetic field for particle tracking at large angles, (b) act as a Møller electron shield, and (c) provide a highly uniform field at the magnet center for the operation of dynamically polarized proton and deuteron targets. Fig. 10 shows the moment when the magnets had reached their full design currents.
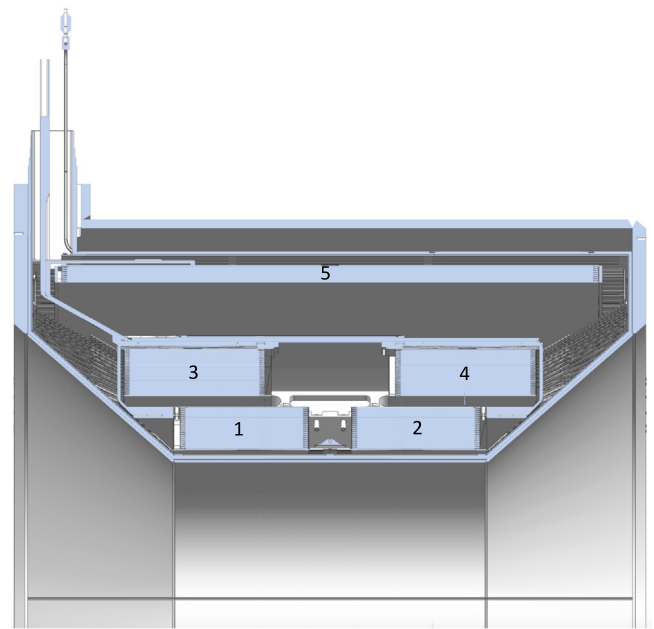
Fig. 9. Cut view of the upper half of the solenoid coils with the four 2 × 2 main coils on the inside, and the shield coil (5) on the outside. The shield coil provides effective compensation for the magnetic field sensitive photomultiplier tubes that are located just outside of the magnet cryostat (not shown). The nominal field in the center of the magnet is 5 T.

Fig. 11 shows the correlation of solenoid field strength vs. current up to (and slightly beyond) the maximum current.

The magnet consists of 4 cylindrical coils arranged in two packages at different radial distances to the beamline. A fifth coil is located outside of the 4 inner coils and generates a magnetic field in the opposite direction of the field of the 4 inner coils and thus acts as an active magnetic shield. The number of turns in the main coils is 3704 ($2 \times 840 + 2 \times 1012$) and in the shield coil is 1392. The magnet is powered at a nominal current of 2416 A. At full current the solenoid generates a 5 T magnetic field at its center. The integrated field length along the magnet center is $\int B dl = 7.0$ Tm, generating a stored energy of 20 MJ. The magnet has an inner warm bore of 78 cm diameter where all of the central detectors are placed. For details on the design and operation of the solenoid magnet, see Ref. [7].

4. The CLAS12 forward detector (FD)

4.1. Drift chamber (DC)

The six coils of the torus magnet mechanically support the forward tracking system, which consists of three independent DCs in each of the six sectors of the torus magnet. Each of the six DC sectors has a total of 36 layers with 112 sense wires, arranged in 3 regions (R1, R2, and R3) of 12 layers each. In each of the six torus sectors the DCs are arranged identically. As displayed in Fig. 12, the R1 chambers are located at the entrance to the torus magnetic field region, the R2 chambers are located inside the magnet where the magnetic field is close to its maximum, and the R3 chambers are placed in a low magnetic field space just downstream of the torus magnet. This arrangement provides independent and redundant tracking in each of the six torus sectors. Each of the 3 regions consists of 6 layers (called a superlayer) with wires strung at a stereo angle of +6° with respect to the sector midplane and 6 layers (a second superlayer) with wires strung at a stereo angle of −6° with respect to the sector midplane. This stereo view enables excellent resolution in the most important polar angle (laboratory scattering angle), and good resolution in the less critical azimuthal
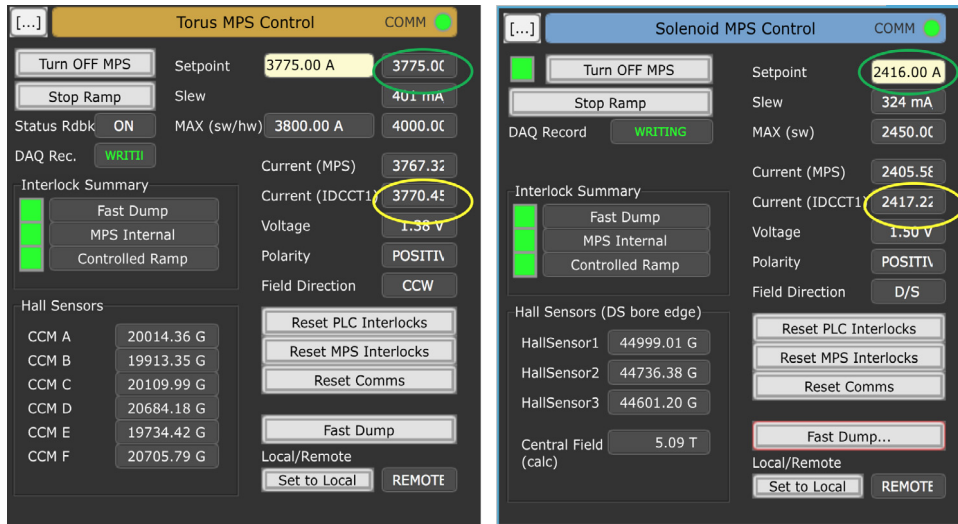
Fig. 10. Energization of the torus magnet (left) and the solenoid magnet (right) to full current.
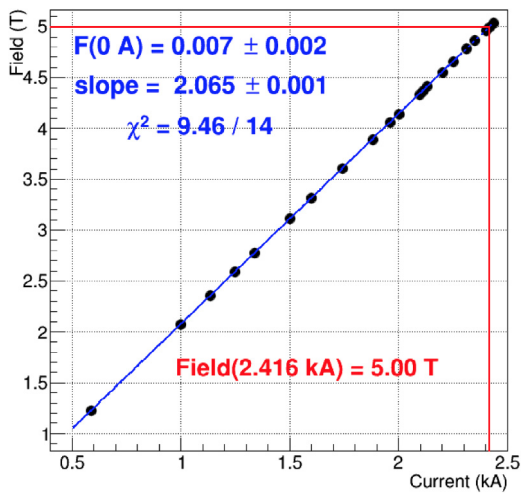

Fig. 11. The excitation line of the solenoid to full current. The nominal field in the center of the solenoid magnet is 5.0 T.

scattering angle. Fig. 13 shows the wire stringing operation for the large R3 chambers. For details of the DC construction and performance, see Ref. [8].

4.2. Particle identification

Cherenkov counters, time-of-flight detectors, and electromagnetic calorimeters are located downstream of the tracking system to provide particle identification and energy measurements for electrons, high-energy photons, and neutrons. Each is described in more detail in the remainder of this section.

4.3. High threshold Cherenkov counter (HTCC)

The HTCC is the main detector to separate electrons (positrons) with momenta below 4.9 GeV from charged pions, kaons, and protons. The detector has full coverage of 360° in azimuth and spans from 5° to 35° in polar angle. It has no blind areas in its complete solid angle coverage. The detector is located downstream of the production target, sandwiched between the solenoid magnet and the torus magnet, in front of the forward tracking detectors.
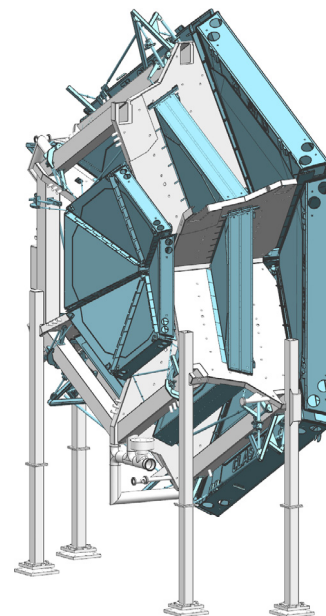
Fig. 12. Drift chamber system in the CLAS12 forward tracking system from the design model. The small-size R1 chambers are located just in front of the torus magnet coils (gray shade). The medium-size R2 chambers are sandwiched between the coils of the magnet, and the large-size R3 chambers are located just downstream of the magnet.

The HTCC system is required to provide high rejection of charged pions and low background noise for reliable identification of scattered electrons in a dense electromagnetic background environment. The HTCC is a single unit operated in dry CO_2 gas at 1 atm pressure. It is constructed using a multi-focal mirror of 48 elliptical mirror facets that focuses the Cherenkov light on 48 photomultiplier tubes (PMTs) with quartz windows of 125 mm diameter. The PMTs are located in a magnetic field of up to 35 G oriented along the phototube axes and are surrounded along their lengths by a multi-layer magnetic shield with active compensation coils.

In order to minimize multiple scattering in the HTCC detector materials and to limit its impact on the momentum analysis of charged tracks in the torus field, the HTCC mirror system is constructed using a backing structure of low-density composite material. As the detector is located in front of the momentum analyzing torus magnet, all materials but the radiator gas in the path of the charged particles had to be

Fig. 13. Simultaneous wire stringing of two R3 chambers in the Jefferson Lab clean room.
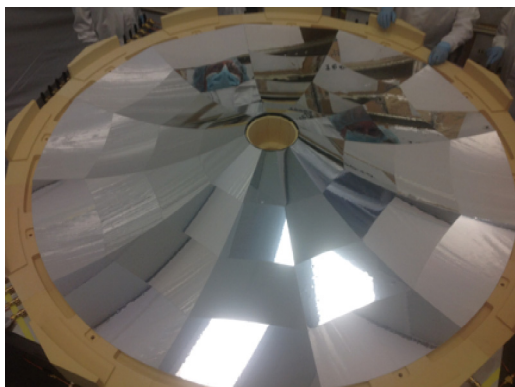

Fig. 14. The HTCC mirror with its 48 mirror facets, each reflecting the Cherenkov light to a different PMT. The mirror spans a diameter of about 2.4 m.

kept to a minimum. In the actual detector, the density of the solid material seen by charged particles passing through the HTCC volume is 135 mg/cm^2.

The HTCC is also used to generate a fast signal to be used as a trigger for scattered electrons. The HTCC operates in conjunction with energy deposited in the electromagnetic calorimeters to identify electrons of specific energies. The 360° mirror system of the HTCC is shown in Fig. 14. Fig. 15 shows a cut view of the assembled HTCC detector. For details of the HTCC construction and performance, see Ref. [9].

4.4. Low threshold Cherenkov counter (LTCC)

The LTCC system is part of the CLAS12 Forward Detector and is used for charged pion detection at momenta greater than 3.5 GeV. The LTCC system consists of boxes shaped like truncated pyramids. Four of the six sectors of CLAS12 are equipped with one LTCC box. Each LTCC box contains 108 lightweight mirrors with composite backing structures, 36 Winston light-collecting cones, 36 125-mm diameter PMTs, and 36 magnetic shields. The LTCC boxes are filled with heavy C_4F_{10} radiator gas. The LTCC system has previously been used to detect electrons in the CLAS detector at lower energies [10]. It has been refurbished to provide higher efficiency for charged pion detection by increasing the volume of the radiator gas, refurbishing the elliptical and
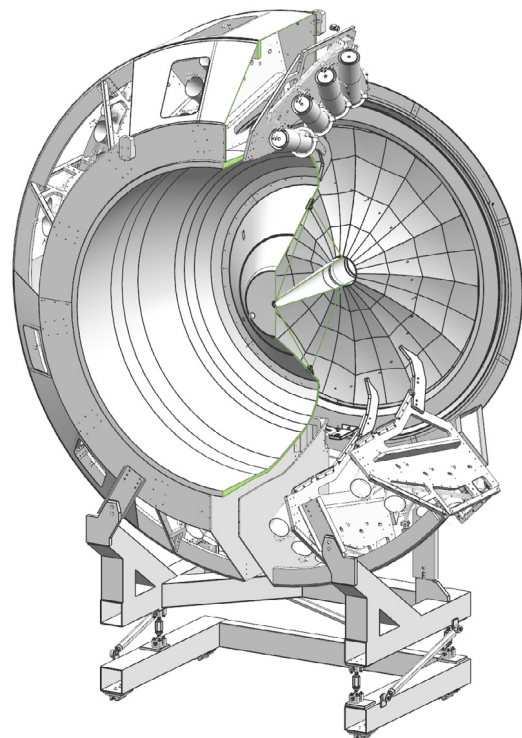
Fig. 15. Cut view of the assembled HTCC detector. The container spans a diameter of about 4.5 m. The mirror is seen at the downstream end to the right. The PMTs are mounted in 12 sectors and in groups of 4 at the outer perimeter of the container. Light collection uses additional Winston cones and 5-in PMTs with quartz windows.

hyperbolic mirrors with new coatings, and improving the sensitivity of the PMTs to Cherenkov light by coating their entrance windows with wavelength shifting material that absorbs ultraviolet (UV) light at wavelength below 300 nm and re-emits two back-to-back photons at larger wavelength. The components of the LTCC optical mirror system and its arrangement are shown in Figs. 16 and 17. For details of the LTCC construction, the detector refurbishment, and its performance, see Ref. [11].
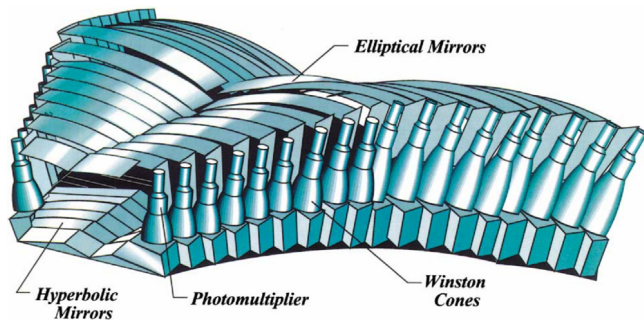
Fig. 16. Layout and components of the optical mirror system within each LTCC box from the design model.
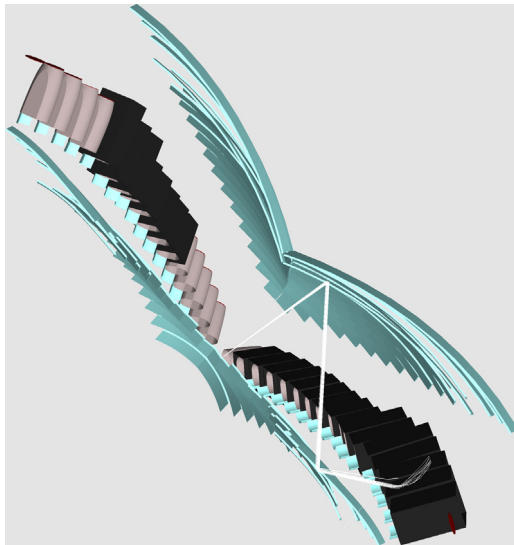

Fig. 17. Perspective representation of the LTCC optical system. A charged particle enters from the bottom left and generates Cherenkov light in the radiator gas volume. The light is reflected off the elliptical mirror array towards the hyperbolic mirror array, from where it is reflected towards the Winston cone and 5-in PMT. The large acceptance coverage requires a complex mirror system for efficient light collection.

4.5. Ring imaging Cherenkov detector (RICH)

Some experiments require the detection and identification of charged kaons in momentum ranges that are not accessible with the standard time-flight method used with the Forward Time-of-Flight system, or with the LTCC Cherenkov counters. The time-of-flight resolution of the scintillators is no longer sufficient to separate kaons from pions for momenta greater than 3 GeV. For that purpose an additional RICH detector was built and incorporated into one of the CLAS12 sectors to replace the corresponding LTCC sector.[1] The RICH detector is designed to improve CLAS12 particle identification in the momentum range 3–8 GeV. It incorporates aerogel radiators, visible light photon detectors, and a focusing mirror system that is used to reduce the detection area instrumented by photon detectors to 1 m^2.

Multi-anode photomultiplier tubes (MaPMTs) provide the required spatial resolution and match the aerogel Cherenkov light spectrum in the visible and near-UV region. For forward scattered particles ($\theta <$ 13°) with momenta 3–8 GeV, a proximity imaging method with thin (2 cm) aerogel and direct Cherenkov light detection is used. For larger incident particle angles of $13° < \theta < 25°$ and momenta of 3–6 GeV, the

---

[1] A second RICH module is presently under construction and will be installed into the final CLAS12 FD sector diametrically across from the first module.
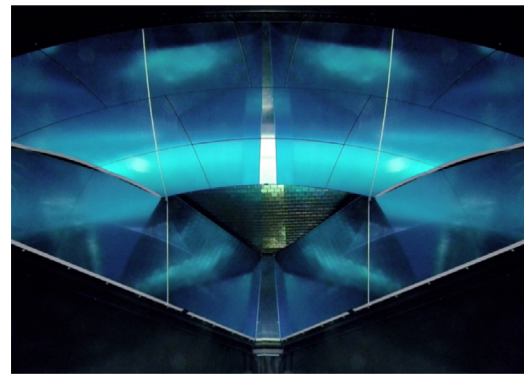

Fig. 18. The RICH mirror system shown here in a perspective view as seen from the entrance window, with the spherical mirrors above, and the planar mirrors below. The detector array with the MaPMTs is seen in the center. The aerogel radiator is not shown.
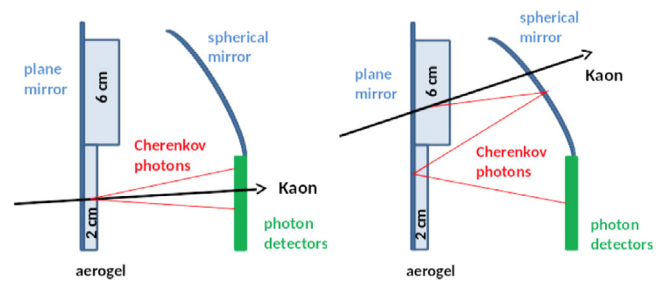

Fig. 19. The principle of operation and the optics of the RICH detector. The left panel shows the optics for direct light detection and the right panel shows the optics for reflected light detection.

Cherenkov light is produced by a thicker aerogel layer of 6 cm, focused by a spherical mirror, and undergoes two further passes through the thin radiator material and a reflection from planar mirrors before detection. Fig. 18 shows the RICH mirror system and Fig. 19 details the optics of the detector. For further details of the RICH detector construction and performance see Ref. [12].

4.6. Forward time-of-flight (FTOF)

The FTOF system is part of the Forward Detector and is used to measure the time-of-flight of charged particles emerging from the production target during beam operation. It includes six sectors of plastic scintillators with double-sided PMT readout. Each sector consists of three arrays of counters (panel-1a - 23 counters, panel-1b 62 counters, panel-2 5 counters). The system is required for excellent timing resolution for particle identification and good segmentation for flexible triggering options. The detectors span a range in polar angle from 5° to 45°, covering 50% in ϕ at 5° and 90% at 45°. The lengths of the counters range from 32.3 cm to 376.1 cm in panel 1a, from 17.3 cm to 407.9 cm in panel-1b, and from 371.3 cm to 426.2 cm in panel-2. The average timing resolution in panel-1a is 125 ps, 85 ps in panel-1b, and 155 ps in panel-2. Figs. 20 and 21 show the FTOF system on the Forward Carriage. For details of the FTOF construction and performance, see Ref. [13].

4.7. Electromagnetic calorimeters (ECAL)

The CLAS12 detector package uses the existing electromagnetic calorimeter (EC) of the CLAS detector [14] and a new pre-shower
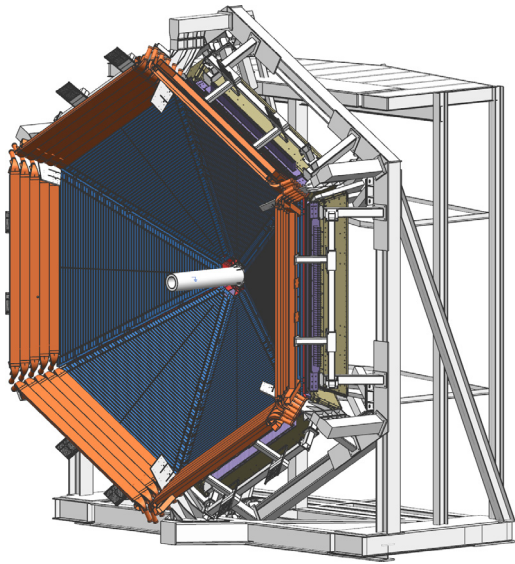
Fig. 20. 3D rendering of the Forward Carriage with the FTOF system showing the panel-1b counters on the inside, and the panel-2 counters on the outside. The panel-1a counters are located immediately downstream of the panel-1b counters and are not visible here. Part of the PCAL is visible downstream of the FTOF panels.
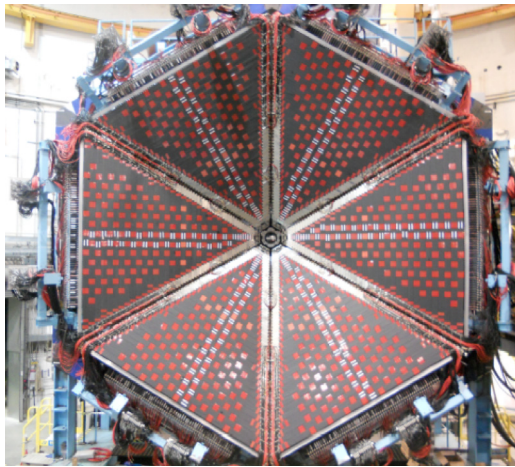

Fig. 21. Photograph of the FTOF panel-1b counters mounted on the CLAS12 Forward Carriage in front of the panel-1a counters and the electromagnetic calorimeters before the installation of the panel-2 counters.

Fig. 22. PCAL after installation on the Forward Carriage in front of the existing EC.

Fig. 23. The Forward Tagger system during cosmic ray testing before installation in CLAS12. The lower part contains the electromagnetic calorimeter composed of lead-tungstate crystals. The upper part includes the hodoscope and the tracking disks. Here the FT is rotated by 90° compared to its installation configuration.

calorimeter (PCAL) installed in front of the EC. Together the PCAL and EC are referred to as the ECAL. The calorimeters in CLAS12 are used primarily for the identification and kinematical reconstruction of electrons, photons (e.g. from $\pi^0 \to \gamma\gamma$ and $\eta \to \gamma\gamma$ decays), and neutrons. For details of the construction of the PCAL and the performance of the ECAL, see Ref. [15].

The PCAL and EC are both sampling calorimeters consisting of six modules. Along the direction from the target, the EC consists of two parts, read out separately, called EC-inner and EC-outer. They provide longitudinal sampling of electromagnetic showers, as well as of hadronic interactions to improve particle identification. Each module has a triangular shape with 54 (15/15/24, PCAL/EC-inner/EC-outer) layers of 1-cm-thick scintillators segmented into 4.5/10-cm (PCAL/EC) wide strips sandwiched between 2.2-mm-thick lead sheets. The total thickness corresponds to approximately 20.5 radiation lengths. Scintillator layers are grouped into three readout views with 5/5/8 PCAL/EC-inner/EC-outer layers per view, providing spatial resolutions of less than 2 cm for energy clusters. The light from each scintillator readout
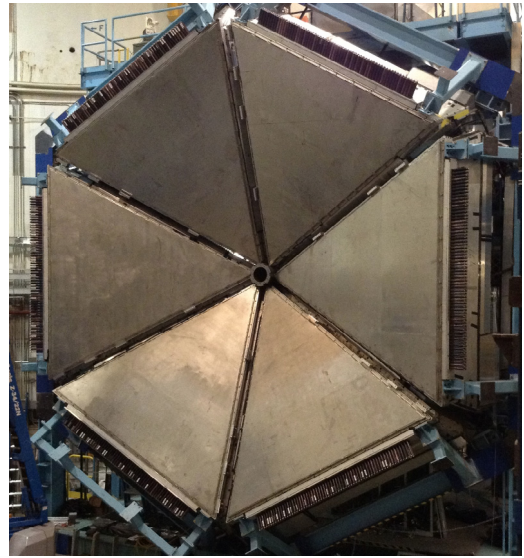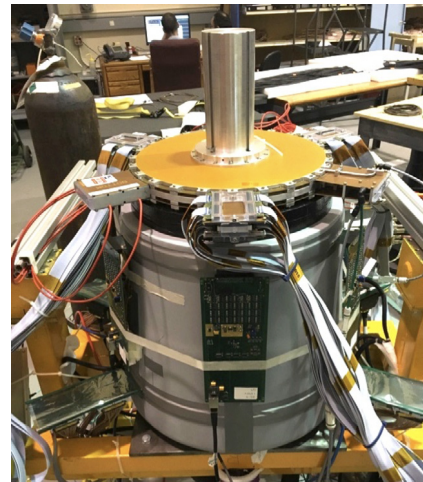
group is routed to the PMTs via flexible optical fibers. Fig. 22 shows the PCAL after installation on the Forward Carriage in front of the existing EC from CLAS.

4.8. Forward tagger (FT)

The Forward Tagger (FT) extends the capabilities of CLAS12 to detect electrons and photons at very forward polar angles in the range from $2.5° \le \theta \le 4.5°$. The detection of forward-going scattered electrons allows for electroproduction experiments at very low photon virtuality Q^2, providing an energy-tagged, linearly polarized, high-intensity, quasi-real photon beam. This configuration enables execution of an extensive hadron spectroscopy program. The FT consists of a calorimeter, a micro-strip gas tracker, and a hodoscope. The electromagnetic calorimeter with 332 lead-tungstate (PbWO$_4$) crystals is used to identify electrons, measure the electromagnetic shower energy, and provide a fast trigger signal. The tracking system in front of the calorimeter measures the charged particle scattering angles, and the scintillator hodoscope aids in separating electrons and high-energy photons.
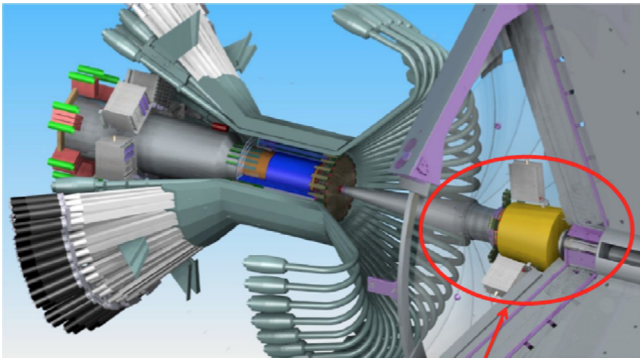
Fig. 24. The Forward Tagger system (circled) downstream of the Central Detector in front of the torus magnet warm bore entrance.
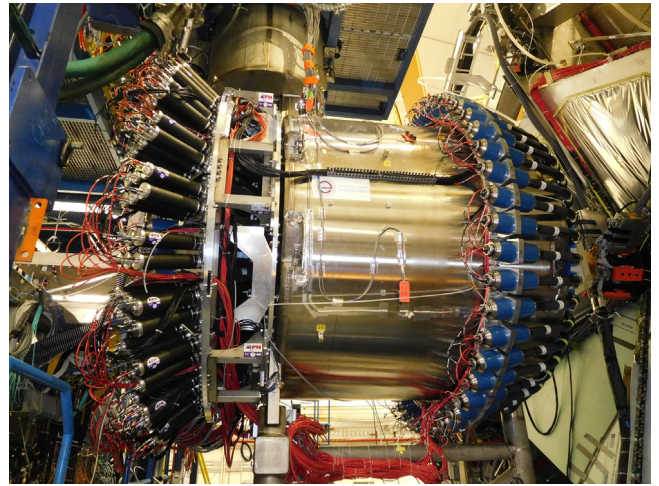

Fig. 25. The Central Detector installed in the solenoid magnet in a side view. The readout PMTs are seen at the upstream end (left) and at the downstream end (right) of the solenoid.

Fig. 23 shows a photograph of the FT during cosmic ray studies before its installation in CLAS12. During beam operations, a tungsten shielding pipe of conical shape is installed in front of the FT to absorb Møller electrons and low-energy photons produced by beam interactions with the target and downstream materials. This shield protects both the FT and the Forward Detectors from electromagnetic background. The cone angle is 2.5°, compatible with the FT acceptance. In this configuration, known as "FT-ON", the FT can be used to detect both electrons and photons, extending the detection capabilities of CLAS12. Alternatively, when the FT is not needed for the physics program, the FT detectors are turned off and additional shielding elements are installed in front of the FT covering up to 4.5° to reduce the background in the DC R1 chambers. This configuration, known as "FT-Off", reduces the accidental background by one-third at the same beam conditions, which allows for higher luminosity data taking with CLAS12. Further details on the FT are described in Ref. [16]. Fig. 24 shows a rendering of the FT setup near the entrance to the warm bore of the torus magnet.

5. The CLAS12 central detector (CD)

Particles scattered from the target at polar angles in the range from 35° to 125° are detected in the Central Detector with its own particle identification and tracking detectors. Charged particles are tracked in the Central Vertex Tracker (CVT) and detected in the Central Time-of-Flight (CTOF) detector with full 360° coverage in azimuthal angle. Neutron detection is provided by the Central Neutron Detector (CND) located radially outside of the CVT and the CTOF. The fully assembled CD is shown in Fig. 25 after installation in the solenoid. Fig. 26 shows the Central Detector from the upstream end.

5.1. Central vertex tracker (CVT)

The CLAS12 CVT is a part of the Central Detector and is used to measure the momentum and to determine the vertex of charged particles scattered from the production target, which is centered within the solenoid magnet. Details of the tracking system are shown in Fig. 27. It consists of two separate detectors, a Silicon Vertex Tracker (SVT) and a Barrel Micromegas Tracker (BMT). The SVT system includes 3 regions with 10, 14, and 18 double-sided modules of silicon sensors instrumented with the digital readout ASIC Fermilab Silicon Strip Readout (FSSR2). The readout pitch is 156 μm, and the total number of channels is 21,504. See Ref. [17] for details on the design, construction, and performance of the SVT.

The BMT contains 3 layers of strips along the beamline and 3 layers of circular readout strips around the beamline, with a total number of 15,000 readout elements. The BMT provides important improvements in momentum resolution and in tracking efficiency. Each layer is arranged azimuthally in 3 segments of 120° azimuthal coverage each. The system operates at the full design luminosity of 10^{35} cm^{-2}s^{-1}.
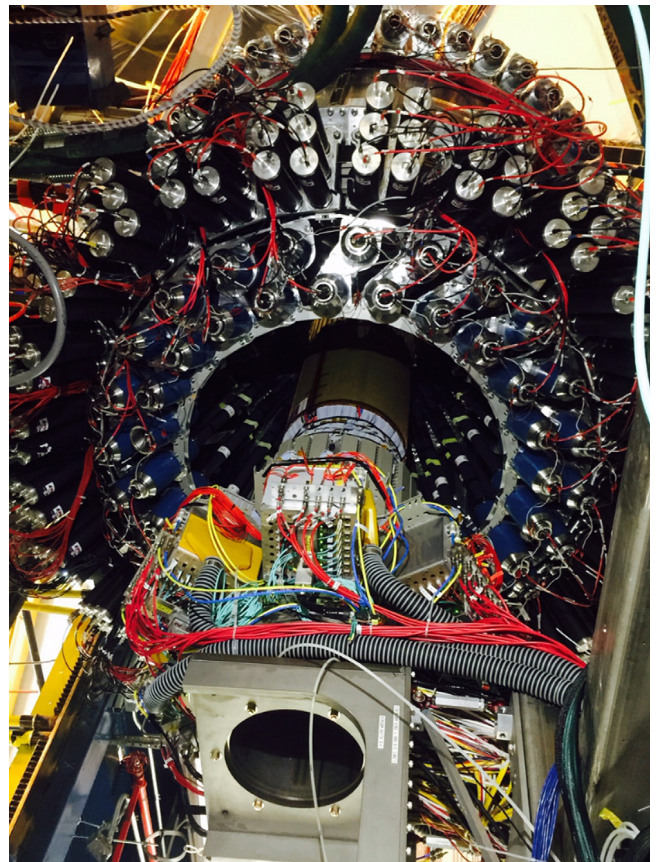
Fig. 26. The Central Detector seen from the upstream end. The central tracker system is shown in a retracted position for maintenance. During operation it is fully inserted into the warm bore of the magnet.

Another component of the CVT is the Forward Micromegas Tracker (FMT), consisting of 6 layers with 6000 readout elements. It is integrated mechanically with the CVT to provide a compact tracking system, but covers the polar angle range from 5° to 35° and provides improved vertex reconstruction for forward-scattered charged particles. The fully assembled CVT, including the FMT, are shown in Fig. 28. See Ref. [18] for details on the BMT and on the FMT.
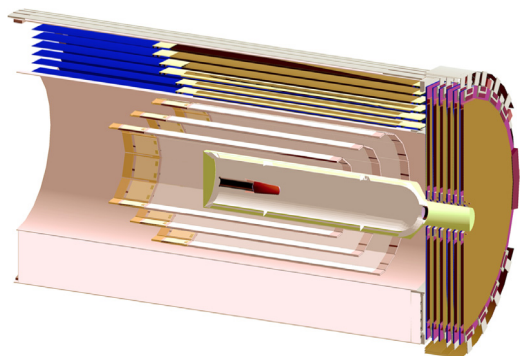
Fig. 27. Central Vertex Tracker schematic, showing (from the inside) the target cell and vacuum chamber, the 3 double layers of the SVT, followed by the 6 layers of the BMT. The beam enters from the left. The six FMT layers are shown at the downstream end at the right.
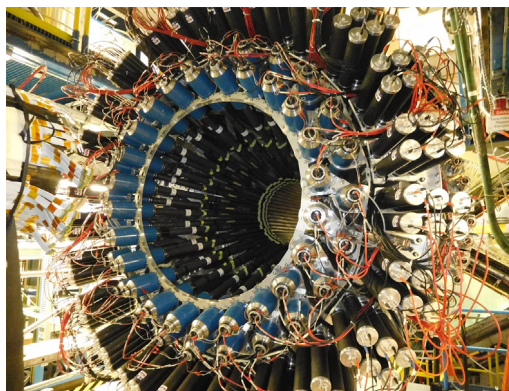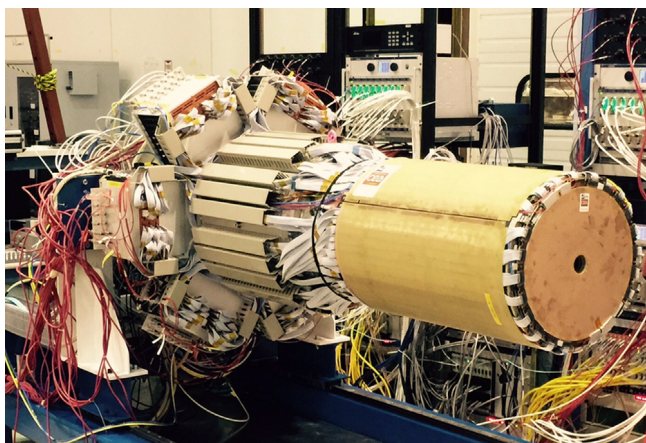

Fig. 28. The fully assembled Central Vertex Tracker with the SVT, BMT, and FMT. The BMT and FMT are shown on the outside. The FMT has a circular opening in the center for the electron beam to pass through. The SVT is encapsulated and hidden from view.
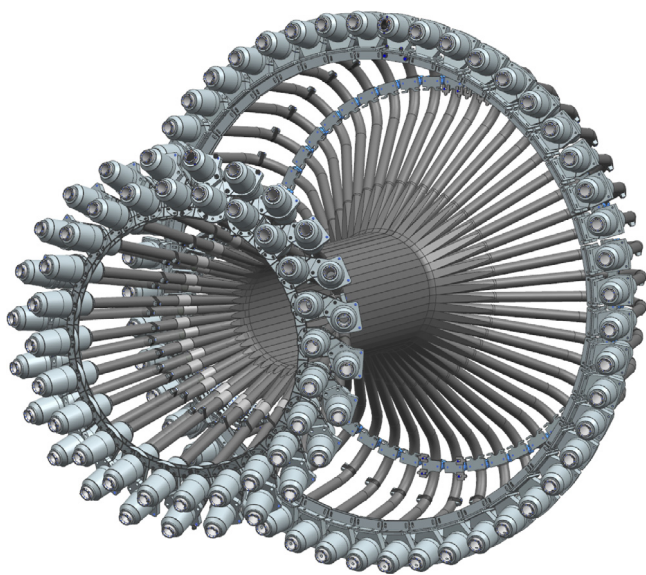

Fig. 29. The CTOF detector with its 48 scintillator bars outfitted with light guides, PMTs, and magnetic shields at both ends of each counter.

Fig. 30. The fully assembled CD as seen from its upstream end with the 144 CND light guides and PMTs at the three outermost rings, and the 48 PMTs of the CTOF (two inner rings).

5.2. Central time-of-flight (CTOF)

The CTOF system is used for the identification of charged particles emerging from the target via time-of-flight measurements in the momentum range from 0.3 to ~1.25 GeV. The CTOF includes 48 plastic scintillators with double-sided PMT readout via, respectively, 1.0-m-long upstream and 1.6-m-long downstream focusing light guides. The array of counters forms a hermetic barrel around the target and the CVT. The barrel is aligned with the beam axis inside the 5 T solenoid magnet. The PMTs are placed in a region of 0.1 T fringe field of the solenoid and enclosed within a triple layer dynamical magnetic shield [19] that provides less than 0.2 G internal field near the PMT photocathode. The CTOF system is designed to provide time resolution of 80 ps for charged particle identification in the CLAS12 Central Detector. Details of the CTOF are described in Ref. [20]. Fig. 29 shows the CTOF system from the design model and Fig. 30 shows the upstream end of the CTOF installed inside the solenoid.

5.3. Central neutron detector (CND)

The CLAS12 CD is also equipped with the CND positioned radially outward of the CTOF that allows the detection of neutrons in the momentum range from 0.2 to 1.0 GeV by measurement of their time-of-flight from the target and the energy deposition in the scintillator layers. The detector is made of three layers of scintillator paddles (48 paddles per layer), coupled two-by-two at the downstream end with semi-circular light guides and read out at the upstream end by PMTs placed outside of the high magnetic field region of the solenoid. The scintillators are connected to 1-m-long bent light guides. Fig. 30 shows the upstream readout end of the CND installed in the solenoid. Details of the CND are described in Ref. [21].

5.4. Back angle neutron detector (BAND)

Neutron detection at back angles is accomplished with the BAND, which is positioned 3 m upstream of the CLAS12 target to detect backward neutrons with momenta between 0.25 and 0.7 GeV. It consists of 18 horizontal rows and 5 layers of scintillator bars with PMT readout on each end to measure time-of-flight from the target. There is an additional 1 cm scintillation layer for vetoing charged particles. The detector covers a polar angle range from 155° to 175° with a design neutron detection efficiency of 35% and a momentum resolution of about 1.5%. Details will be provided in Ref. [22].
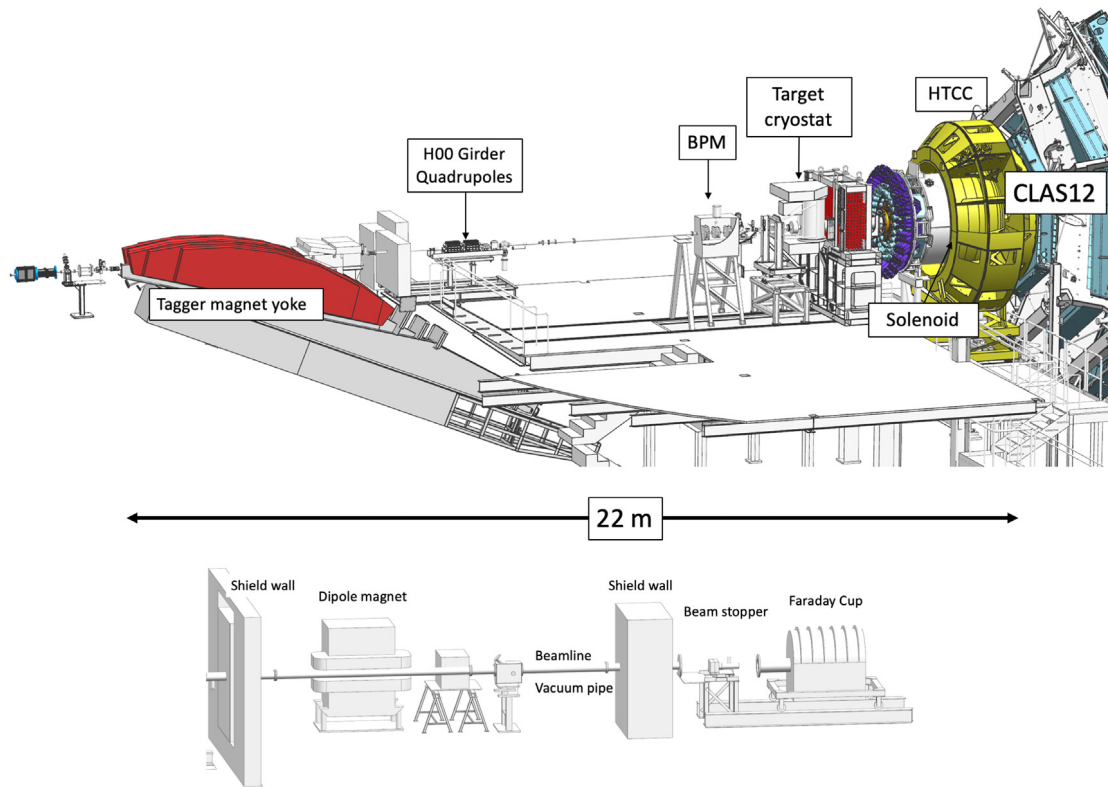
Fig. 31. Top: Hall B beamline upstream of the target, showing the tagger magnet (red) to the left, which is energized during beam tuning and during polarization measurements. The doublet seen downstream of the tagger is a pair of quadrupoles. The beam position monitors (BPMs) are used for beam position and beam current measurements. The main element on the right is the solenoid magnet nearly fully encapsulated by the HTCC (yellow). Several of the torus magnet coils are visible at the far right. Bottom: The part of the beamline that extends from the downstream end of CLAS12 to the Faraday cup, a total absorbing device that is used to integrate the beam current to get the total accumulated charge. (For interpretation of the references to color in this figure legend, the reader is referred to the web version of this article.)

6. Hall B beamline

The Hall B beamline has two sections, the 2C line, from the beam switch yard (BSY) to the Hall proper, and the 2H line, from the upstream end of the experimental Hall to the beam dump (or Faraday cup) in the downstream tunnel. Fig. 31 shows the portion of the 2H line from the tagger dump magnet to the entrance to CLAS12 and the portion of the 2H line downstream of CLAS12 leading to the Faraday cup.

The beamline instrumentation consists of beam optics, beam position and beam current monitors, beam viewers, collimators, shielding, beam profile scanners, and beam halo monitors. Devices that control the beam direction, its profile, and measure critical parameters, are under the accelerator operations control. Hall B operators control collimators, halo monitors, profile scanners, and viewers. They are also responsible for configuration and running the Møller polarimeter located upstream of the tagger magnet.

The tagger magnet on the left of Fig. 31 (in red) is not energized during production data taking. When energized the yoke of this magnet serves as a beam dump that is used during beam tuning before the beam is directed on the Hall B production target. It is also used during specialized runs, such as polarization measurements in the upstream beamline, to avoid exposure of sensitive CLAS12 detectors to high background loads. For details of the beamline elements and beam quality, see Ref. [23].

The performance of the electron beam and all diagnostic elements in the beamline, status of the beamline vacuum, the superconducting magnets, and the rates in all detector systems that are indicative of potential beam quality issues are directly displayed on a single master screen that is accessible to the shift personnel and other experiment-related personnel and experts. Fig. 32 shows the details of the monitoring screen.

6.1. Monte Carlo simulations

A critical part of operating an open large-acceptance detector system at high luminosities is the simulation not only of hadronic events but also, and more importantly, the simulation of the beam-related accidental hits in the tracking systems. The source of accidentals is primarily from the beam electron elastically scattering off atomic electrons (Møller electrons) and their secondary interaction with beamline components. The production rate is orders of magnitude larger than the hadronic production rate. These background sources have to be shielded through careful design of magnetic channeling, as well as a proper design and careful optimization of the beamline shielding and the vacuum pipe to minimize interaction of these electrons with high-Z material. The availability of a realistic simulation package was essential for the optimal design of the CLAS12 integrated detector concept.

The strong solenoid field is essential in channeling the scattered Møller electrons through the beam enclosure to avoid interactions with the beamline materials. Fig. 33 shows a single randomly triggered event at 50% of full luminosity in a time window of 250 ns. This corresponds to the time window in the R1 drift chambers used in the event reconstruction. The main conclusion is that only when both magnets are energized can the detector be operated with acceptable background levels (see Fig. 33 lower left). Additionally, a realistic simulation package is essential for the normalization of cross sections, especially to take into account the detector occupancies for data taking at luminosities near or above the maximum design luminosity where the track reconstruction efficiency can be significantly affected by accidentals. In order to quantitatively account for this, data were taken at different beam currents (i.e. different luminosities) with randomly triggered events. Data from these randomly triggered events were merged with simulated physics events to study the loss of real tracks
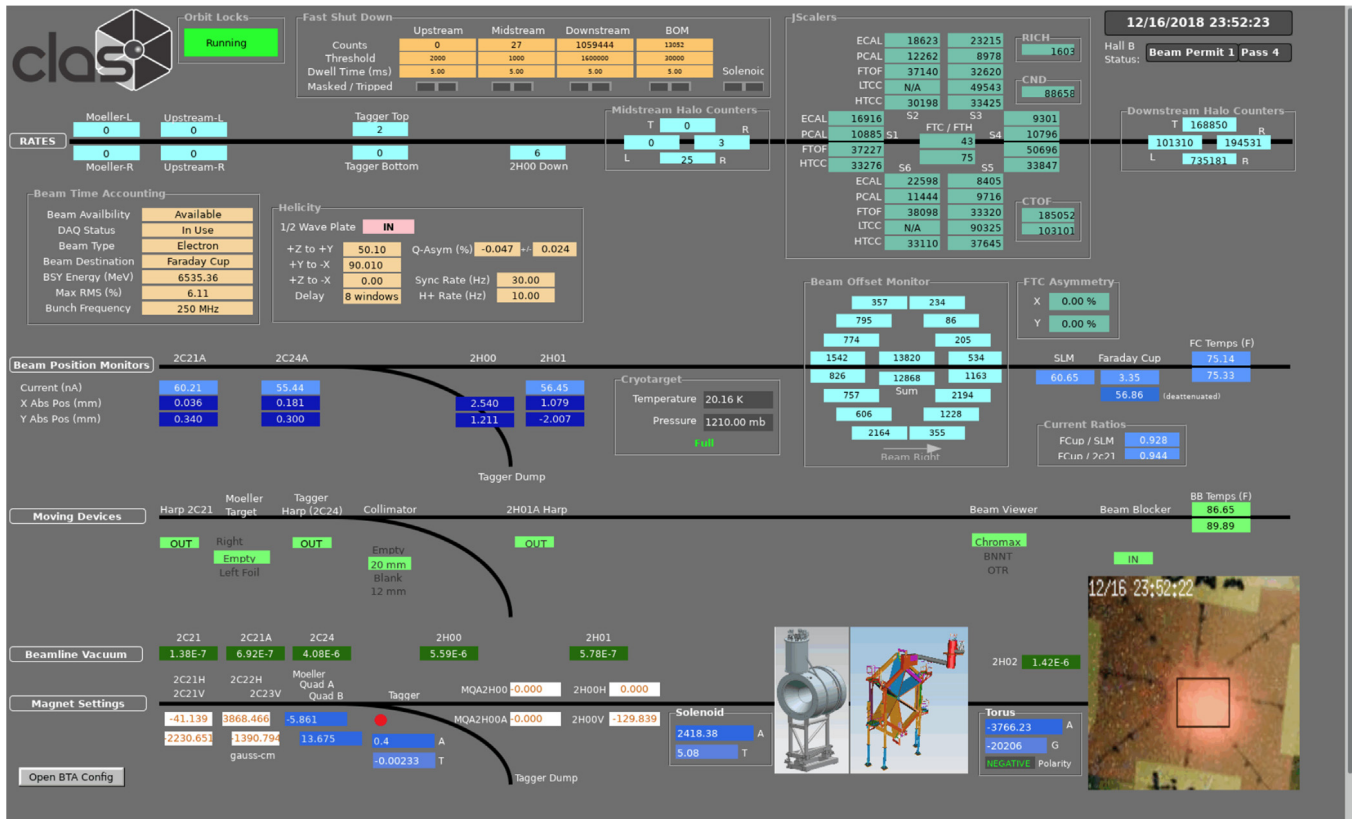
Fig. 32. The CLAS12 beamline and detector monitoring systems in Hall B. Top line (left to right) shows the beam halo counters (that typically have zero or single digit rates if the beam quality is good), detector integrated rates in all six sectors, and halo counter rates downstream of the target. Second line: beam position and beam current monitors, status of the cryogenic target, beam offset monitor (16 counters around the beam just upstream of the target), and Faraday cup information. Third line: Devices that can be moved in and out of the beam used for beam viewing and profile measurements, and polarization measurements with Møller scattering. Fourth line: Beamline vacuum conditions, beamline quadrupole settings, CLAS12 torus and solenoid settings, Chromax beam viewer, and beam blocker in front of the Faraday cup.

for different data runs. See Ref. [24] for details on the CLAS12 Geant4 simulation package GEMC.

6.2. Experimental targets

Hall B experiments are grouped into running periods with similar beam energy, detector configuration, magnet settings, and target material. The most common target materials have been liquid hydrogen and liquid deuterium. Other materials include solid nuclear targets of various kinds from ^{12}C to ^{208}Pb, depending on the physics requirements. For some specialized experiments high-pressure gas targets are used. All targets are positioned inside CLAS12 using support structures that are inserted from the upstream end, and are independent of the detector itself.

A large science program with CLAS12 requires the use of spin-polarized protons and neutrons. Spin-polarized protons and polarized neutrons are used in compound materials where the hydrogen or deuterium can be spin polarized using microwave-induced electron spin transitions in molecules such as in NH_3 and ND_3. Certain electron spin–flips can be transferred to the proton or neutron in the hydrogen or deuterium atoms, and lead to high polarization of up to 90% for the free protons and over 50% in neutrons of the deuterium atoms in this process of dynamical polarization. To achieve high levels of polarization, a high magnetic field of 5 T is required. In CLAS12, the required magnetic field is externally provided by the 5 T field in the center of the solenoid magnet, which has been designed to provide a homogeneous magnetic field of $\Delta B/B_0 \leq 10^{-3}$ within a cylindrical region of diameter $\phi = 2.5$ cm and $\Delta z = 4$ cm along the beamline. The region near the target cell includes additional correction coils to achieve a factor of 10 better homogeneity that is needed for polarizing the deuterium nuclei

in ND_3. Other polarized materials, such as polarized HD (called HD-Ice), will also be used in support of programs that require spin-polarized targets with the polarization axis oriented transverse to the direction of the electron beam.

7. Data acquisition and trigger system

7.1. CLAS12 data flow and monitoring

During data taking the quality of the data is continuously monitored by displaying a very small fraction of single events in the CLAS12 event display (*ced*) that allows immediate action by the shift personnel in case of any malfunctioning detector elements or electronics modules. Monitoring histograms are also filled on a regular basis that include detector subsystem channel occupancies, as well as simple analysis plots and can be easily compared with results collected earlier during the data taking.

The CLAS12 data acquisition (DAQ) system is designed for an average of 20 kHz Level 1 (L1) trigger rate, pipelined for continuous operation. The sector-based L1 triggers support data streaming, subsystem hit patterns, and energy summing with low threshold suppression. The scalable trigger distribution scheme uses 111 front-end L1 crates. CLAS12 uses different programmable features for each detector that participates in the L1 trigger. A schematic diagram showing a complete overview of the DAQ system is shown in Fig. 34. In 2018 the DAQ was run at trigger rates of typically 15 kHz and data rates of up to 500 MB/s with a livetime of >95%. At somewhat lower livetime of ~90%, trigger rates of 20 kHz and data rates of up to 1 GB/s have been achieved. Details of the design, functionality, and performance of the CLAS12 DAQ are provided in Ref. [25].
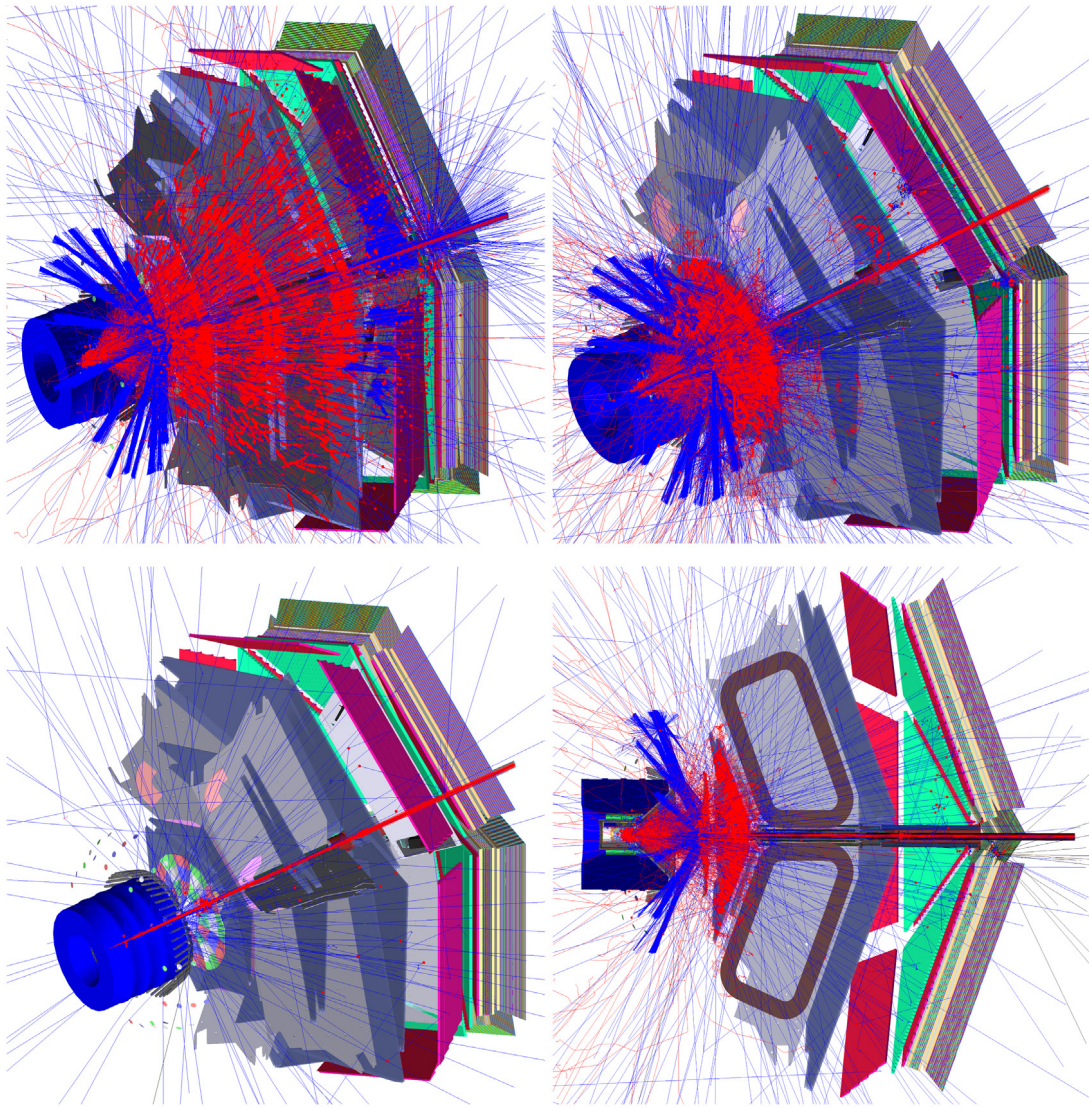
Fig. 33. Geant4 representations of accidental background events occurring within a 250 ns time window at different magnetic field configurations and at 50% of design luminosity. Top left: Solenoid field is OFF and torus field is OFF. Top right: Solenoid field is OFF and torus field is ON. Bottom right: Rotated 2D view of top right. Bottom left: Solenoid field is ON and torus field is ON. Color code: red lines are primary electrons; red circles are hits in the detectors; blue lines are photons, including the Cherenkov light, which is clearly visible as the narrow light bundles just at the downstream end of the solenoid magnet, created by the Møller electrons in the HTCC when the solenoid magnet is OFF.

7.2. Fast and selective triggers

CLAS12 uses a series of fast triggers that are tailored to a specific event pattern selection. Most of the physics experiments require the electron scattered on the production target to be detected as it defines the mass (Q^2) and kinematics of the virtual photon as $Q^2 = -(e - e')^2$, where e and e' are the 4-momentum vectors of the beam electron and of the scattered electron, respectively. The scattered electron is uniquely identified with signals in the HTCC and clustered energy deposition in the ECAL.

At the nominal design luminosity of CLAS12, the hadronic production rate is approximately $5 \times 10^6/s$. However, only a small fraction of the events is of interest for the science program with CLAS12. In particular, most physics reactions require the detection of the scattered electrons at some finite scattering angle, for example $\theta_{e'} > 5°$. Fig. 35 shows one example of an electron-triggered event with one additional positively charged track. The trigger purity depends on the polarity of the torus magnet and on the beam-target luminosity. Only about 50% of the electron triggers recorded with an inbending torus polarity are actually electrons. For the outbending torus polarity, the electron trigger purity is as high as 70%. In trigger definition list, charged

particles in either the FD or the CD can also be selected in the trigger in addition to the scattered electron making use of the detector responses.

In some experiments the detection of electrons in the FT is of interest if they are associated with hadronic event patterns of one or two additional detected hadrons. Such conditions have been implemented in the fast trigger decision that reduces the number of triggers to about 2×10^4 events/s, i.e. by a factor of 250 from the hadronic rate. The data rate is typically 500 MB/s under such conditions and can be handled by the CLAS12 data acquisition system and the available computing resources. Fig. 36 shows an example of specific triggers configurations that have been used during the fall 2018 run period. Details of the design, functionality, and performance of the CLAS12 trigger system are provided in Ref. [26].

8. CLAS12 offline software

The CLAS12 offline event reconstruction is designed to analyze large amounts of beam-induced experimental data acquired during production and cosmic ray runs; the latter being used for alignment and calibration purposes. The CLAS12 reconstruction framework is built based on a service-oriented software architecture, where the
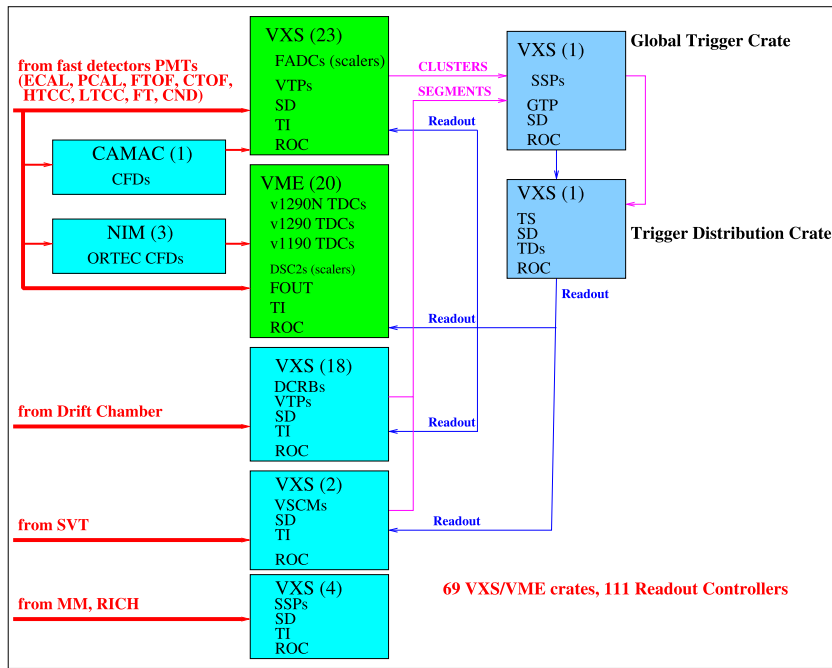
Fig. 34. Schematic diagram of the CLAS12 data acquisition and trigger system.
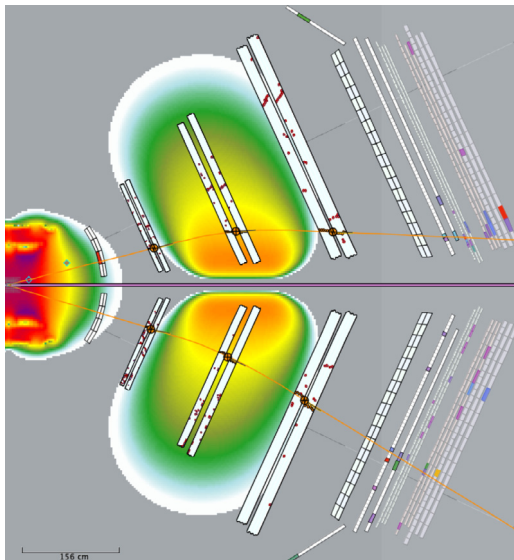

Fig. 35. View of an event in CLAS12 from the *ced* event display. Predefined trajectories from a look-up table are employed to select hit patterns in the 3 DC regions that correspond with localized energy deposition in the ECAL. For the two-track trigger, the two sectors show DC hit patterns for tracks with opposite charges. The upper track is an electron, shown by the hit in the HTCC that bends towards the beamline. The lower track has positive charge and bends away from the beamline.
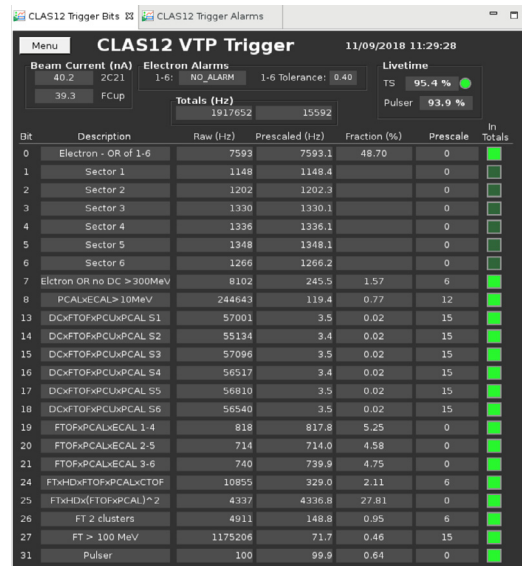
Fig. 36. The CLAS12 trigger control screen during a specific data run with a total of 17 active triggers operating at a livetime of 95.4%. Nearly half (48.7%) of all triggers are from single electrons detected in one of the 6 FD sectors. Over a quarter (27.81%) of all triggers required an electron in the FT with an additional two charged hits detected in the FTOF and in the PCAL. Several others were taking data at the 5% level and required charged tracks in the FTOF and ECAL in opposite FD sectors. Finally, several other triggers were used for monitoring purposes and were heavily pre-scaled.

reconstruction of events is separated into micro-services that execute data processing algorithms. The software packages consist of the event reconstruction, visualization, and calibration monitoring services, as well as detector and event simulations.

During the CLAS12 design phase a realistic simulation package based on Geant4 was developed to aid in the optimization of the detector hardware response to beam interactions in terms of resolution, robustness of operation at high luminosity, details of the beamline design, and other aspects.

8.1. Event reconstruction

Event reconstruction in the CLAS12 FD consists of the identification of charged and neutral particles along with the determination of their 3-momenta and reaction vertex at the distance of closest approach to the beamline. Charged particle reconstruction requires both forward tracking and FTOF information.

Track reconstruction in the FD is based on a hit clustering algorithm that requires at least 4 out of 6 connected DC cells to form a track
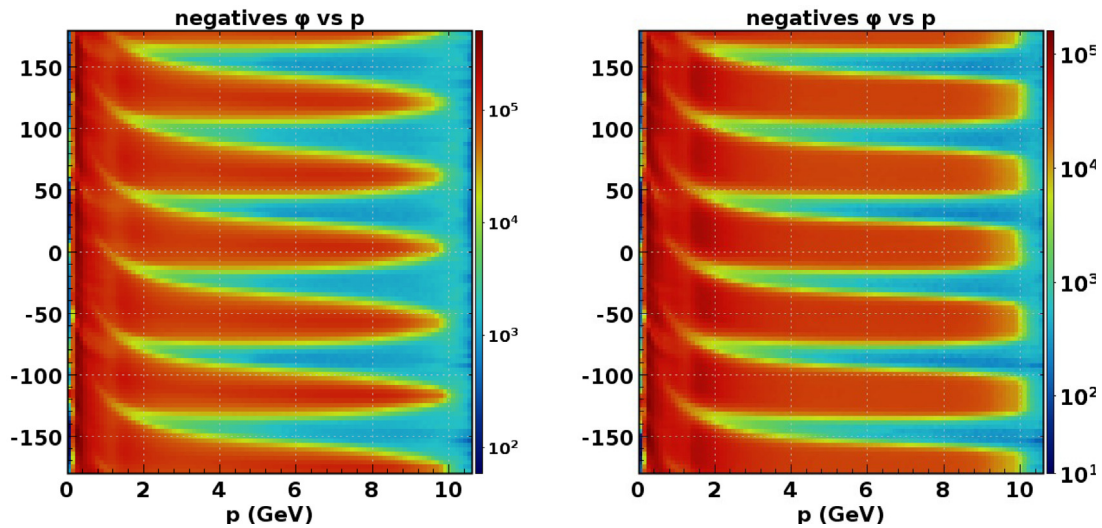
Fig. 37. Particle distributions in azimuthal angle (ϕ) vs. momentum in the CLAS12 FD for inbending electrons (left) and with reversed torus field for outbending electrons (right) at a beam energy of 10.6 GeV. The azimuthal angle is measured at the production vertex. The azimuthal distribution of inbending electrons narrows with increasing momentum, as high-momentum electrons in CLAS12 are bent towards the beamline, where detector acceptances are reduced. This is not the case for outbending electrons that are deflected away from the beamline toward larger detector acceptances. The $p - \phi$ correlation, most visible at low momentum, is due to the solenoidal magnetic field that bends charged tracks dependent on their transverse momentum component and on their charge. For positively charged tracks the ϕ motion is in the opposite direction from negative (electron) tracks. Color axes indicate the particle yields. (For interpretation of the references to color in this figure legend, the reader is referred to the web version of this article.)
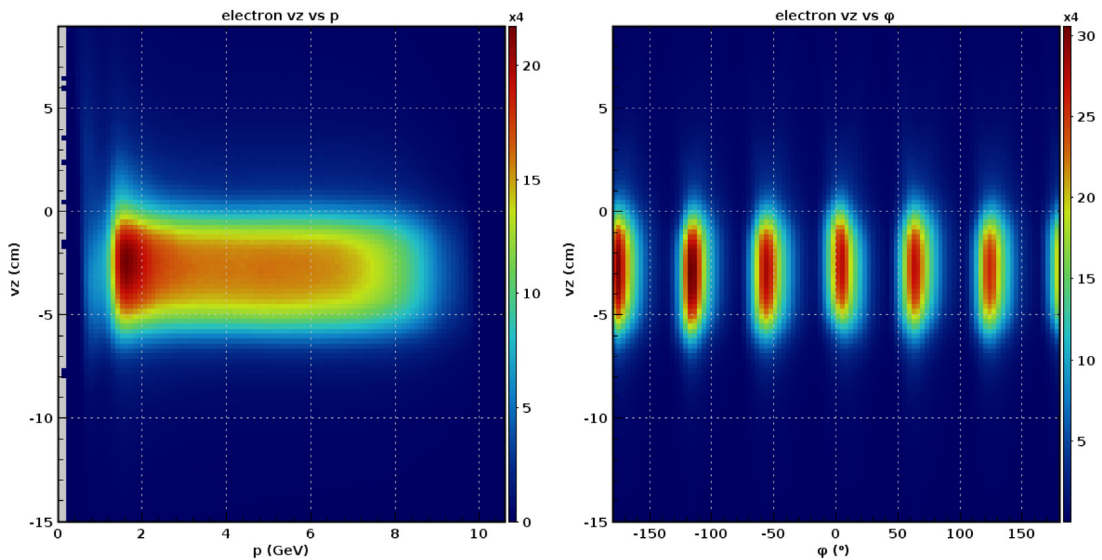
Fig. 38. Reconstructed vertex along the beamline vz for electrons in the FD. Left: vz vs. momentum, Right: vz vs. azimuthal angle. The vertical size of the vertex band is consistent with the target length of 5.0 cm.

segment within each superlayer. The tracking algorithm requires at least 5 out of 6 superlayers in a sector to form a track candidate. The first stage of tracking relies solely on the DC wire positions to fit the tracks and to provide matching to the outer detectors subsequently required to obtain timing information. At the second stage of tracking, timing information is used to determine a time-based track and the particle momentum and flight path, while the FTOF gives the particle velocity (β) when combined with flight-path information (see Ref. [27] for details). The momentum and velocity information are combined to give the particle mass: $m = p/\beta\gamma$. Electron identification additionally requires the track to match in time and position with both an HTCC hit and an isolated shower in the ECAL. The energy of the shower must be consistent with the track momentum measured by the DCs in the torus magnetic field.

Charged particles are tracked in each sector separately using the 3 regions of DCs in each sector. Most tracks are confined within one

sector as the magnet optics and the massive mechanical support of the torus coils prevent most tracks from crossing from one sector into a neighboring sector. In rare cases low-momentum charged pions can cross from one sector into the opposite sector traversing through the beam pipe. Such tracks are not reconstructed but they are included in the event simulation. Distributions of charged particles in azimuthal angle vs. momentum are shown in Fig. 37. Fig. 38 shows the production vertex as reconstructed in the FD tracking system (from data where the FMT was not installed). As the tracking detectors in each sector are independent of each other, they have to be independently aligned and calibrated. The reconstructed vertex is independent of the sector and also independent of the electron momentum, is an indication that the tracking detectors are well aligned.

Neutral particles are detected in either the calorimeters or in the FTOF (or both). The reconstruction begins by finding isolated clusters of energy, and determining the spatial location, deposited energy, and
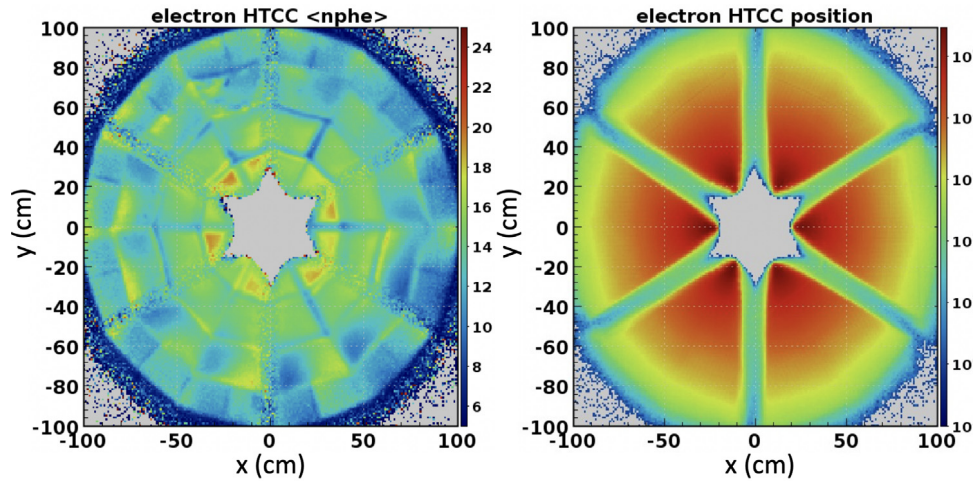
Fig. 39. Distribution map of the number of photoelectrons collected in polar and azimuthal angle of the HTCC shown in terms of the y vs. x transverse coordinates. The plot is based on measurements with a trigger threshold of 2 photoelectrons. The averaged electron detection efficiency is estimated at greater than 99% in the full phase space covered by the HTCC. In localized areas, in particular at interfaces of different mirror facets or between mirror sectors, the efficiencies can be as low as 94%. This map enables bin-by-bin corrections for absolute normalization. Right panel: Distribution of electrons from forward tracking reconstruction at the HTCC location in polar and azimuthal angle. The gaps between sectors are due the scattered electrons being lost in the torus coils and not reconstructed.
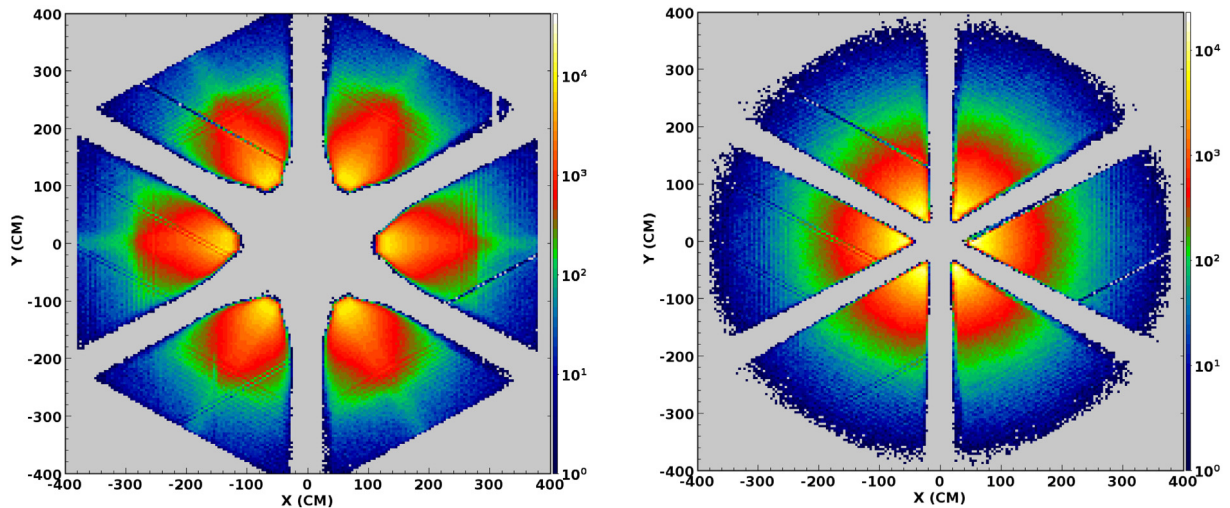
Fig. 40. Distribution of electron track y vs. x coordinates propagated to the PCAL front face (as seen from the target). The few empty strips are due to hardware issues. (Left) Data for electrons bent away from the beamline (outbending). Right: Data for electrons bent toward the beamline (inbending).

the time of the cluster. Neutral particle candidates are identified as clusters in the outer detectors (FTOF, PCAL, EC) that do not match any charged particle track. For high-energy photons that deposit all of their energy in the calorimeters, the energy is calculated from the signal pulse height in the calorimeters. The momenta of neutrons are computed from their flight time as determined by the timing signal in the calorimeters and, when relevant, the matched FTOF counter. In either case, the angle of the neutral particle trajectory is determined from the position of the cluster at a depth in the ECAL that minimizes parallax effects associated with tracks that are not normal to the face of the ECAL (see Ref. [15] for details).

For all events, precise determination of the interaction time or event start time is required. For events where the scattered electron is detected, the event start time is derived from the arrival time of the electron at the FTOF counters, corrected for flight path and signal delays. The average time resolution for electrons reconstructed in the CLAS12 FD is better than 80 ps. A more accurate event start time is obtained by replacing the measured electron start time with the 499 MHz accelerator RF signal (or 249.5 MHz depending on the accelerator setup) that determines the beam bunch associated with the event. In

this way, the event start time can be determined to within ∼20 ps, thus eliminating a significant contribution to the time resolution smearing for charged hadrons. This extends the charged particle identification capabilities of CLAS12 towards higher particle momentum.

Track reconstruction in the CD is generally less complex as tracks are determined fully by the geometry of the detection elements and the hit pattern in the CVT, i.e. by a combination of the SVT and the BMT trackers. In contrast to the charged particle tracking in the FD that relies heavily on timing information for resolution, this is not the case for the CD. In principle, that makes tracking easier in the CD. On the other hand, the redundancy of track fitting is much reduced in the CD as there are only 12 tracking layers compared to the 36 in the FD. This makes tracking in the CD more susceptible to losing tracks due to accidental hits. Charged particle identification in the CD is given by the timing information in the CTOF (or CND) scintillators combined with the track momentum measured in the strong solenoid magnetic field.

Neutral particles are detected in the CD in the CND or the CTOF (or both). As for the FD, neutral particle candidates are identified as clusters that do not match any charged particle track. See Ref. [27] for
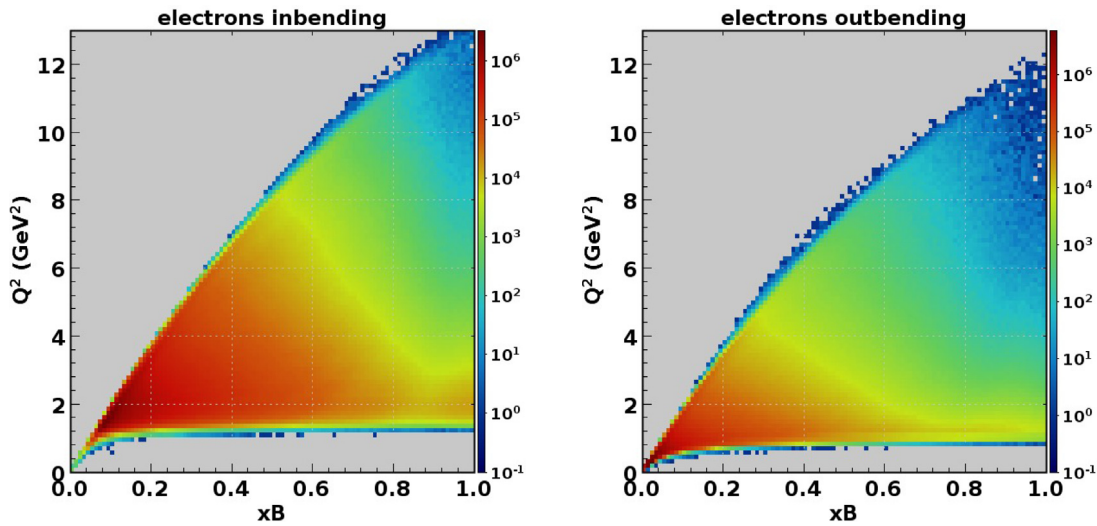
Fig. 41. Inclusive $ep \rightarrow e'X$ coverage in Q^2 vs. x_B at a beam energy of 10.6 GeV. The full kinematics is measured simultaneously. The kinematic range is given by elastic scattering kinematics at $x_B = 1$, and the small angle acceptance at the Q^2 limit for scattered electrons bending (left) toward the beamline (inbending) or (right) away from the beamline (outbending). The two configurations require opposite directions of currents in the torus magnet coils. Note that the minimal Q^2 is lower for the electron outbending configuration, and that the maximum Q^2 reach is slightly higher for inbending electrons.
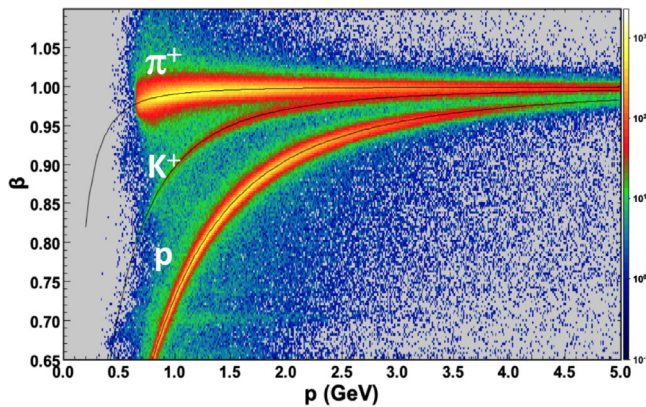
Fig. 42. $\beta = v/c$ vs. momentum of positively charged particles detected in the CLAS12 FD. Events were selected to have an electron identified. The charged particle trajectories are reconstructed and their path length and timing from the target to the FTOF (panel-1b layer) are determined. The start time at the target is given by identifying the corresponding beam bucket as time t=0. The thin black lines show the expected distributions for the respective charged tracks. Particle identification is limited to momenta greater than 0.8 GeV when the torus magnet is energized to maximum current. At reduced torus current the tracking is extended to lower momenta at the expense of momentum resolution.
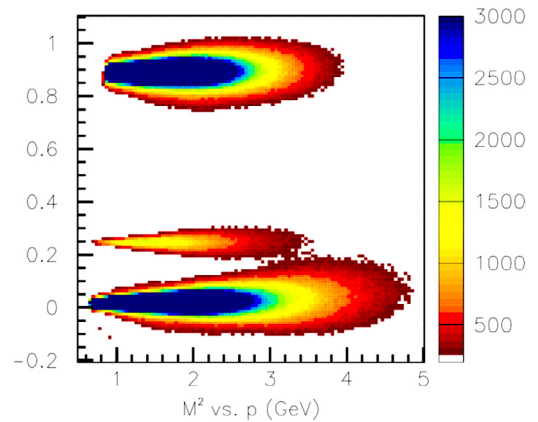

Fig. 43. Reconstructed mass squared vs. momentum of positively charged particles in the CLAS12 FD. The same data are used as in Fig. 42. However, the plot contains a threshold on the minimum and maximum number of events per bin to eliminate background events between the particle bands, and to better visualize the scarce kaons in the particle samples, which are of special significance for the science program. Bottom: π^+, middle: K^+, top: p. The centroids of each particle distribution are approximately independent of the momentum. Masses are computed from the particle path length and from time-of-flight. Any momentum dependence would indicate systematics in the timing calibration or in the path length determination.

9. CLAS12 operational performance

This section describes the overall performance of the CLAS12 detection system. Most of the experimental programs require the clean identification and reconstruction of the scattered electron. Electrons are identified by a combination of signals in the HTCC and energy deposited in the combined electromagnetic calorimeters PCAL and EC, with a matched negatively charged track in the DC tracking system. Of critical importance is the response of the HTCC that operates between the CD and the entrance to the DC system. The reconstructed electron coordinates at the HTCC are shown in Fig. 39(right), exhibiting a very uniform distribution in azimuthal angle. The distribution of photoelectrons across the entire 48 segments of the HTCC active region is shown

in Fig. 39(left), which exhibits a rather uniform and high efficiency for electrons over its full acceptance.

The coordinates of the reconstructed electrons at the front face of the PCAL are shown in Fig. 40 for electrons bending towards the beamline, and with reversed torus magnetic field with electrons bending away from the beamline. The different appearance of the two plots is the result of the difference in optics for the two configurations. The distributions are rather uniform in all six sectors, showing that the detector systems and the reconstruction software are working properly. The few empty strips indicate malfunctioning detector elements or electronics modules. The acceptances for the inbending and the outbending scattered electron show quite different features. Outbending electrons hit the ECAL front face significantly further out radially than inbending electrons do. This is a feature of the magnetic field of the torus magnet. Also, the outer acceptance bounds are quite different. In the outbending case, they are defined by the ECAL geometry, while for the inbending
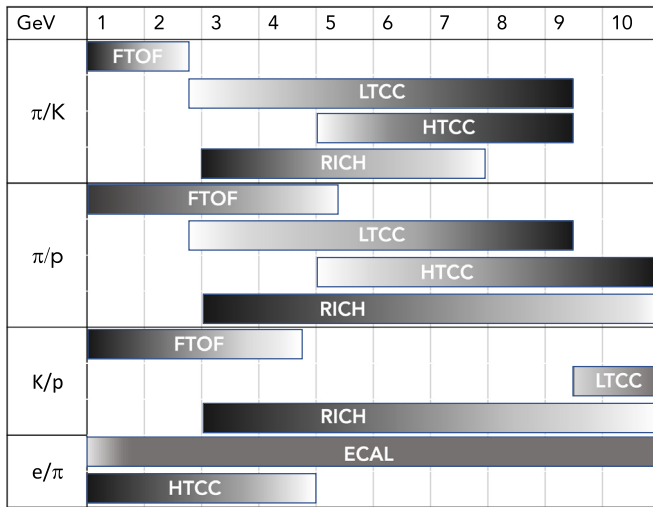
Fig. 44. Overview of the different detector subsystems in the CLAS12 FD used for particle species separation vs. momentum. Darker shading corresponds with higher sensitivity.

case the acceptance bounds are given by the HTCC geometry, as can be seen in Fig. 39.

Elastic scattering of electrons on protons allows for the establishment of any deviations from the ideal detector geometry and alignment. The coverage in kinematical quantities Q^2 and x_B of the scattered electrons detected in the FD is shown in Fig. 41. Q^2 is the virtuality of the photon exchanged from the electron to the proton target and x_B

is the Bjorken scaling variable (defined as $Q^2/(2M E_\gamma)$, where M is the target mass and E_γ is the energy of the virtual photon exchanged with the target). The electron kinematics also define the invariant mass W defined as $W^2 = M^2 + 2M\nu - Q^2$, with $\nu = E_e - E_{e'}$ and M the mass of the target particle. For inbending electrons the coverage in Q^2 is up to 13 GeV^2 at $x_B \approx 1$, while for the outbending electrons it is limited to $Q^2 \approx 12$ GeV^2.

9.1. Charged particle detection in the FD

Charged particle yields in momentum and azimuthal angles are shown in Fig. 37 in the local sector frame for positively and negatively charged particles. The difference in the acceptance is due to two factors, the polarity of the torus magnet that bends negative particles away from the beamline and positive particles towards the beamline (or vice-versa for the opposite torus polarity), and the effects of the solenoid magnetic field that causes an azimuthal motion for positive and negative particles in opposite directions.

Identification of charged particles in CLAS12 is achieved in a number of ways. Identified electrons are used to determine the hadron start time at the production vertex. The start time and the path length of charged tracks from the production vertex to the FTOF and the FTOF hit time, enable the determination of the velocity ($\beta = \upsilon/c$) of the particle, shown in Fig. 42 vs. particle momentum for positively charged tracks. The computed mass squared vs. momentum for these tracks is shown in Fig. 43. An overview of the detector subsystems in the CLAS12 FD used for the identification of the different charged particle species vs. momentum is shown in Fig. 44.

Fig. 45 shows the inclusive invariant mass W spectra for $ep \to e'X$ and missing mass spectra for $ep \to e'\pi^+X$ with a missing neutron at four different beam energies. Fig. 46 shows the invariant mass of $\pi^+\pi^-$.
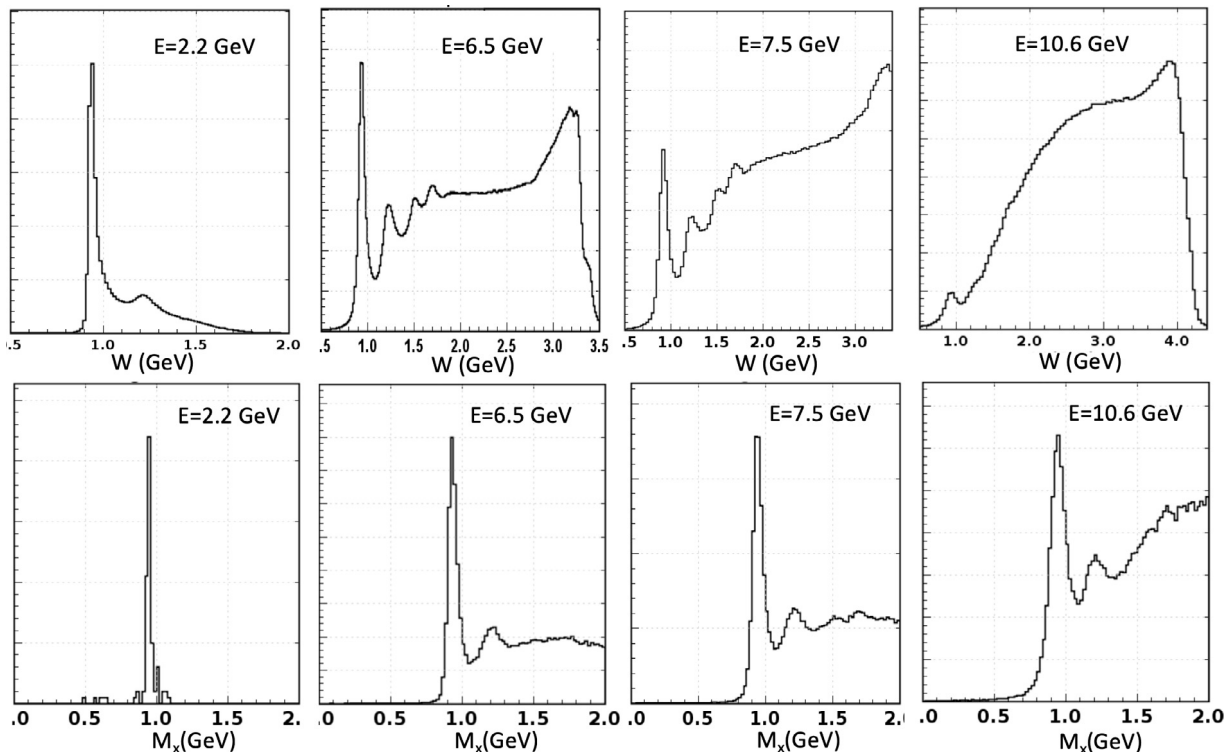

Fig. 45. Upper row: Inclusive electron scattering spectrum $ep \to e'X$ measured in CLAS12 at beam energies of 2.2 GeV, 6.5 GeV, 7.5 GeV, and at 10.6 GeV (from left to right). The peak to the left is due to elastic $ep \to ep$ scattering. Enhancements from the first 3 excited nucleon states, $\Delta(1232)$, $N(1520)$, and $N(1680)$, are also visible for the lower beam energies. Note that the mass ranges are different for the different beam energies. Lower row: Missing mass distributions of $ep \to e'\pi^+X$ for the same energies. The sharp mass peak to the left is due to the undetected neutron. The second peak for the higher energies is due to the $\Delta^0(1232)$. Indications of higher mass neutron excitations are also visible.
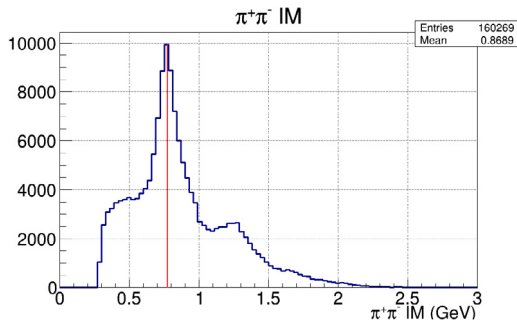
Fig. 46. Invariant mass of $\pi^+\pi^-$ at 10.6 GeV beam energy. The vertical line indicates the mass of the $\rho^0(770)$ meson. The shoulder to the right is from the $f_2(1270)$ meson.
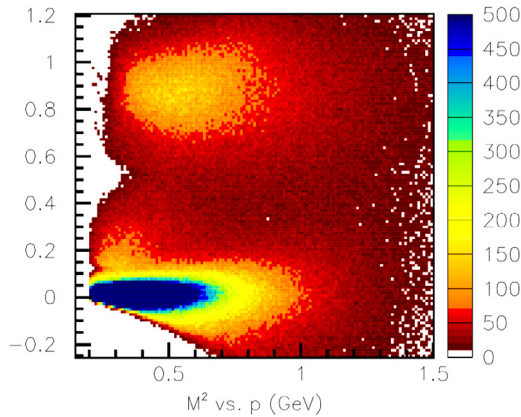

Fig. 47. Mass squared of positively charged particles evaluated from their path length and the time-of-flight information in the CTOF vs. the particle momentum at 10.6 GeV beam energy. The band at the bottom is from π^+, the faint band near 0.2 is from K^+, and the band at the top is from protons. The momenta are not corrected for energy loss in the CVT.
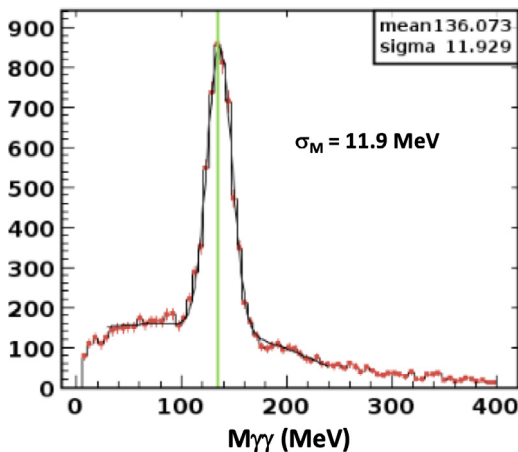
Fig. 48. The invariant mass of two high-energy photons in Sector 4 of the ECAL from 10.6 GeV beam data. The background beneath the π^0 peak is due to multi-photon decays of higher-mass mesons where one or more photons are not detected in the angle range covered by the calorimeter. The width (σ) of the mass peak is 11.9 MeV, which is in good agreement with the Monte Carlo simulations in Ref. [27]. The energy calibration of the calorimeter uses cosmic ray muons.

9.2. Charged particle detection in the CD

Momentum reconstruction in the CVT combined with the timing information from the CTOF allows for the separation of charged pions, kaons, and protons in the momentum range from 0.3 GeV to 1.25 GeV.
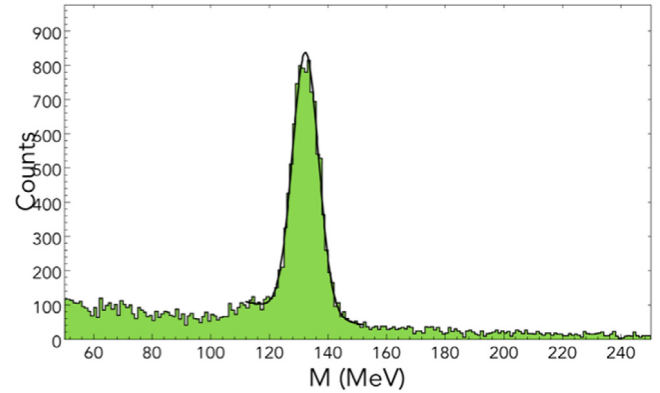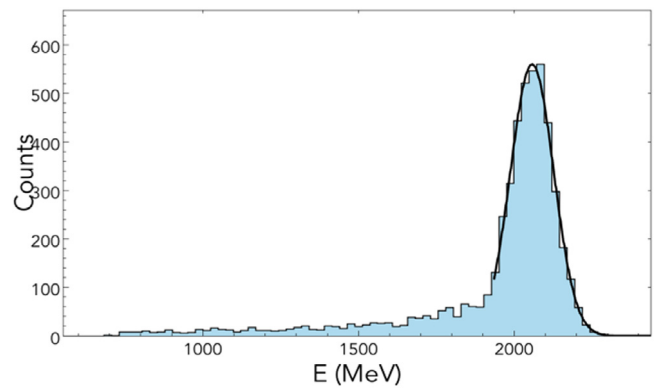

Fig. 49. Top: The energy response of the FT calorimeter to elastically scattered electrons at 2.2 GeV beam energy. The tail at lower energies is due to radiative effects. The energy resolution is $\sigma_E/E \approx 3.3\%$. Bottom: 2γ mass for photons detected in the FT lead-tungstate crystal calorimeter. The π^0 mass resolution is $\sigma_{\gamma\gamma} = 4.4$ MeV, which is somewhat larger than the Monte Carlo simulation resolution of ≈ 3.5 MeV.

This momentum range covers a large part of the phase space allowed by the maximum beam energy for hadron electroproduction on hydrogen targets. Fig. 47 shows the reconstructed mass squared vs. particle momentum reconstructed in the CVT.

9.3. Neutral particle detection

Direct detection of neutral particles is accomplished in the FD using the PCAL and EC calorimeters. The combined 20 radiation lengths are sufficient to identify high-energy photons and reconstruct the masses of the parent particles, such as $\pi^0 \rightarrow \gamma\gamma$ or $\eta \rightarrow \gamma\gamma$. At very forward angles the FT provides photon detection with significantly improved position and energy resolution in the polar angle range from 2.5° to 4.5°. Fig. 48 shows the invariant mass of the $\gamma\gamma$ system in the CLAS12 FD. The energy response of the FT to 2.2 GeV electrons and the $\gamma\gamma$ mass resolution are shown in Fig. 49.

Neutral particle detection in the CD is provided by the CND combined with the CTOF. The plastic scintillator bars of the CND have an $\approx 12\%$ nuclear interaction length, resulting in a $\approx 10\%$ efficiency for the detection of high-energy neutrons. The plastic scintillators contribute about 29.6% of a radiation length at $\theta = 90°$; hence they also detect high-energy photons through their conversion into e^+e^- pairs. The discrimination of photons and neutrons in the CD is accomplished by the timing resolution of 80 to 100 ps provided by the CTOF and the 160 ps of the CND. The separation of neutral particles from charged particle hits in the CND or in the CTOF is efficiently achieved by using the CVT tracker to veto against false neutral hits in the CTOF and CND. Fig. 50 shows the velocity vs. the energy deposition of charged and neutral particles in the CND. The measured neutron detection efficiency is shown in Fig. 51.
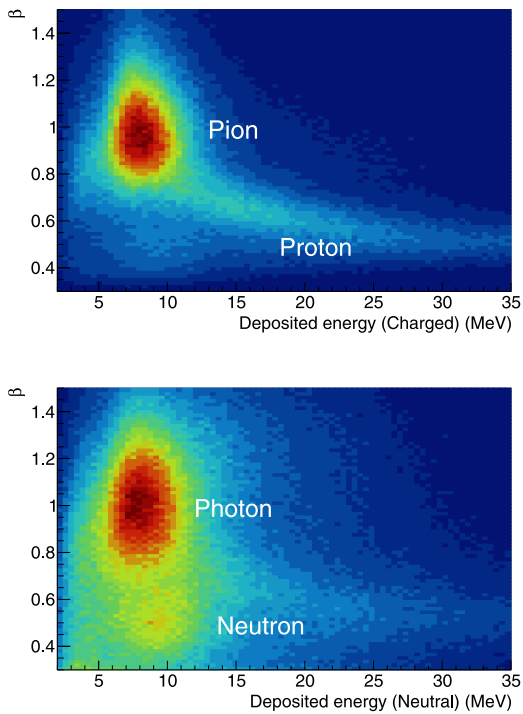
Fig. 50. Top: Distribution of $\beta = v/c$ for charged particles in the CND vs. the deposited energy for correlated charged tracks in the CVT. Evidence for charged pions and protons is clearly visible. Bottom: The same for neutral particles; no charged tracks are correlated with the energy deposited in the CND scintillators.
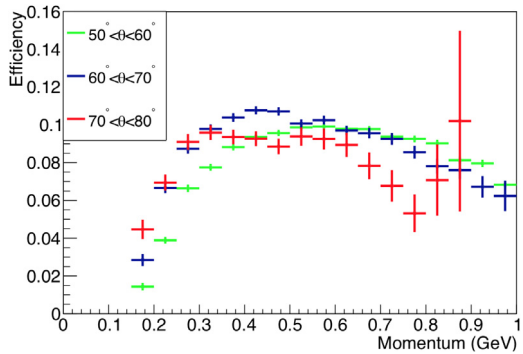

Fig. 51. The neutron detection efficiency in the CND vs. momentum for different polar angles. The detection efficiency has been measured using the reaction $ep \rightarrow e'\pi^+n$, where the neutron kinematics are given by the other detected particles. The ratio of observed neutron hits to predicted neutron hits in the CND gives the detection efficiency. The efficiency has some angle and momentum dependence as shown.
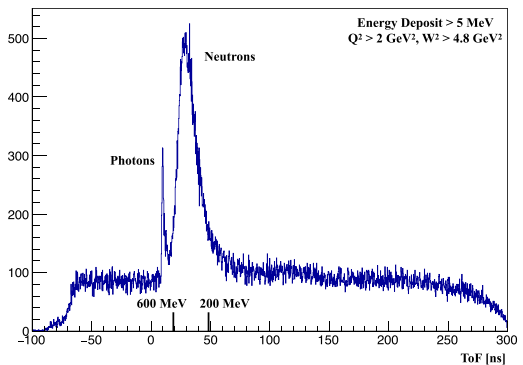

Fig. 52. BAND response to electron-triggered events emerging from a nuclear target at very backward polar angles. Photons and neutrons sitting on accidental background events are well separated by precise timing information.
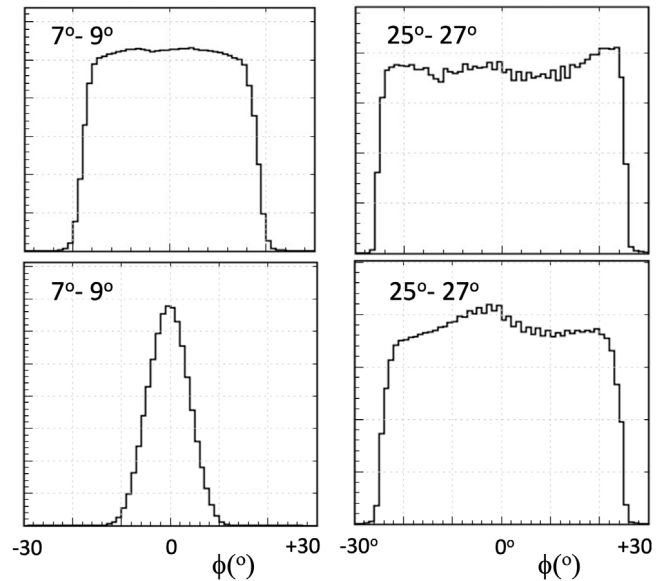

Fig. 53. Yields of electrons in azimuthal angle (in deg.) for two bins in polar angle. Top: Outbending electrons, Bottom: Inbending electrons. Left: $\theta = 7°–9°$. Right: $\theta = 25° − 27°$. The reduced ϕ acceptance at small polar angles is due to the torus coils blocking part of the ϕ coverage, as is seen in Fig. 8). In addition, for inbending electrons the acceptance is further reduced as those electrons bend towards the beamline, where the forward detectors have a smaller extension in azimuth. (The vertical axes are in arbitrary, linear units.).

At far backward angles, the BAND detector provides neutron identification with detection efficiencies up to 35%. As there are no tracking capabilities in the very backward direction, the separation of charged particles is achieved by a veto counter, corresponding to a 1-cm-thick scintillation counter in front of the BAND. The separation of neutrons and photons is achieved by the timing information, which is shown in Fig. 52.

10. Electron beam operation

During beam operation the status of the beamline diagnostics and other critical components, as well as most of the detector components, are continuously monitored. Some of the beamline elements are used to warn of beam conditions that may negatively impact detector operation and are used as a fast shutdown of beam delivery.

10.1. Forward detector reconstruction

The science program with CLAS12 in general requires the detection of electrons that are scattered off the target material. For determining the kinematics of the reaction, the electrons must be identified and their 3-momentum determined by tracking them in the magnetic field of the torus magnet, and detecting them in the FTOF and in the ECAL, which covers approximately the polar angle range from 5° to 35°. The detailed acceptance ranges depend also on the polarity of the torus magnetic field. Charged tracks that are deflected away from the beamline have acceptance functions that are different from charged tracks that are deflected toward the beamline. Fig. 53 shows the distribution of reconstructed electrons vs. azimuthal angle ϕ for different ranges of polar angle θ at 8° and 26° showing the different acceptances for outbending vs. inbending electrons.

The magnetic field of the solenoid also affects the acceptance function of charged particles. For opposite charges but the same momentum, the azimuthal rotation of scattered charged particles is the same in magnitude but opposite in sign. The particle acceptance is a complex function of the phase space covered by the processes of interest and

Table 1
Impact of high-current operation on the resolution of kinematic quantities in single track reconstruction. The resolution parameters are without the use of the FMT tracker, which should significantly improve the v_z-vertex resolution. Note that the highest beam current of 120 nA is 60% higher than the nominal operating value of 75 nA. The resolution values were obtained through single particle simulations at fixed kinematics.

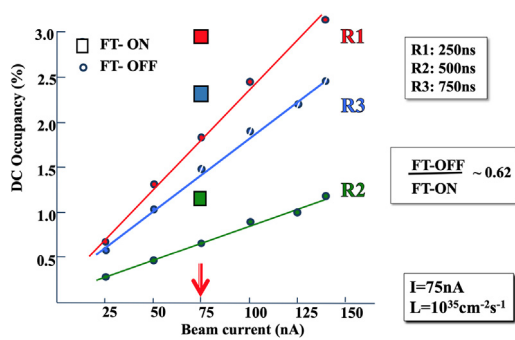| Parameter	Current	Resolution	Specs
$\Delta p/p$ (%)	0 nA	0.52	≤ 1
	60 nA	0.67	
	120 nA	0.86	
$\Delta\phi$ (mrad)	0 nA	3.3	≤ 4.5
	60 nA	3.8	
	120 nA	4.4	
$\Delta\theta$ (mrad)	0 nA	0.66	≤ 1
	60 nA	0.85	
	120 nA	0.85	
Δv_z (mm)	0 nA	3.5	–
	60 nA	4.6	
	120 nA	5.6	

Fig. 54. Accidental occupancies in the three DC regions vs. the beam current with the solenoid magnet at full field. The measurement was carried out in the FT-OFF configuration. The dependence on the beam current is linear. At 75 nA beam current the measurement was also done in the FT-ON configuration (large squares), and the accidental occupancies increase on average by $\approx 62\%$ compared to the FT-OFF configuration. The time windows during data collection were 250 ns for R1, 500 ns for R2, and 750 ns for R3, approximately corresponding to the charge collection times in the DC. The FT-ON configuration results are consistent with the Monte Carlo simulations for R1, but they underestimate the R2 data by 35% and the R3 data by 25% [24,28].

must be simulated in full detail to precisely extract cross sections and other physics observables. For this purpose a full simulation package was developed, based on the software package Geant4 [24].

10.1.1. Luminosity performance during CLAS12 operations

CLAS12 is designed for operation at a luminosity of $L = 10^{35}$ cm^{-2}s^{-1}, which corresponds to a beam current of 75 nA and a liquid-hydrogen target of 5 cm length. The high-luminosity operation has measurable effects on the hit occupancy in the drift chambers and on the resolution in the reconstruction of kinematical quantities. Also, the reconstruction efficiency of charged particles can be affected. Figs. 54 and 55 show the hit occupancies in the drift chambers for different beam currents and for different currents in the solenoid magnet, respectively.

The effects of luminosity on the reconstruction can be studied in simulations when the beam conditions can be realistically imposed on the data. For that purpose a procedure was developed that takes randomly triggered events at the operating beam current and superimposes these events on the simulated events without the background. In this way one can study the reconstruction efficiencies as a function of luminosity of the actual experiment. With increasing luminosity, accidental out-of-time events can affect and alter particle tracks that come in-time. The most important effect is that the track quality is negatively impacted, leading to track losses if stringent quality requirements are
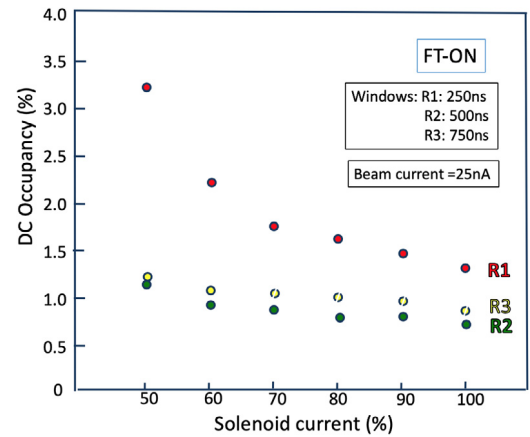

Fig. 55. Hit occupancies in the three DC regions vs. the current in the solenoid magnet. The measurement was carried out in the FT-ON configuration. The sensitivity on the solenoid current comes from the fact that the primary background source is from charged particles, especially Møller electrons. The sensitivity is strongest for DC R1, which have no additional magnetic shielding from the torus magnet field, while the R2 and R3 chambers do.
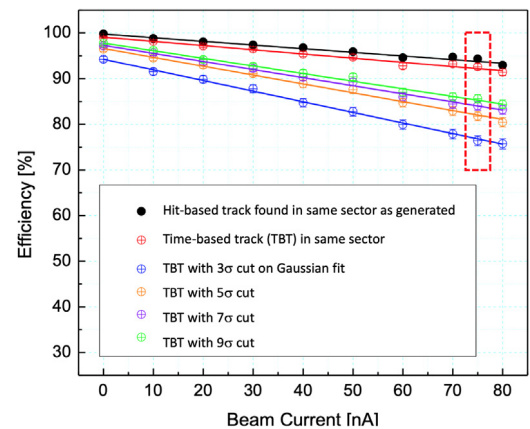

Fig. 56. Single track reconstruction efficiency for simulated muon events vs. luminosity. Here the efficiency is defined as the ratio of the number of reconstructed tracks within the cut window, to the number of generated tracks. The accidental background events were used from randomly triggered data runs taken at the same beam current. The different colored points show the tracking efficiency when certain quality constraints are imposed. About 6%–7% of the tracks are lost at 75 nA beam current corresponding to a luminosity of 10^{35} cm^{-2}s^{-1} with no quality cuts (black: hit-based tracking - HBT, red: time-based tracking - TBT). The other curves show losses in the tracking efficiency when increasingly stringent selection cuts are applied on the width of the missing mass distribution (most stringent for line with steepest slope). Experimental data will be used to determine realistic tracking efficiencies at different experimental conditions. (For interpretation of the references to color in this figure legend, the reader is referred to the web version of this article.)

applied, or to a worsening of the angle and momentum resolution. This effect is demonstrated in Table 1.

Another way of quantifying the effect of accidental background is by studying the percentage of tracks lost when certain track quality requirements are imposed. Detailed simulations must be done for specific operating conditions, such as magnetic field settings, event triggers, beam current, and production targets. As an illustration, an example of such a simulation is shown in Fig. 56. The process simulated was elastic muon–proton scattering (which, of course is not feasible at an electron accelerator), where the proton mass is inferred from the elastic muon track, and compared with the known proton mass. Muons were used as an ideal probe that does not require corrections for radiative effects as electron scattering does. At higher beam currents, increasingly wider tails develop on the inferred proton mass distribution.
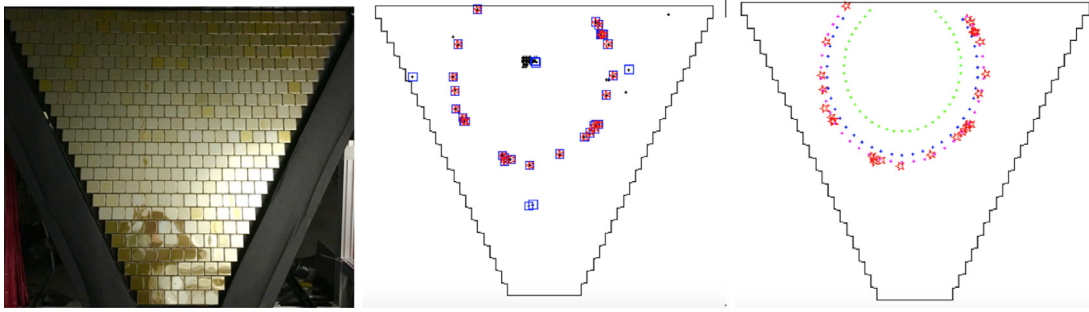
Fig. 57. Photograph (left) and detector response (right) of the RICH MaPMT array during beam operation. Middle: One event with the ring of Cherenkov photons. Right: same event overlaid with expected rings from a pion, kaon, and proton at the same momentum. The radius of the Cherenkov ring is consistent with the outermost circle, which corresponds to a pion.

Table 2
CLAS12 performance parameters based on the current state of the reconstruction, subsystem calibrations, knowledge of the detector misalignments, and the understanding of the torus and solenoid magnetic fields. Resolutions in charged particle momentum and angles were determined from simulations.

Capability	Quantity	Status
Coverage & Efficiency	Tracks (FD)	$5° < \theta < 35°$
	Tracks (CD)	$35° < \theta < 125°$
	Momentum (FD & CD)	$p > 0.2$ GeV
	Photon angle (FD)	$5° < \theta < 35°$
	Photon angle (FT)	$2.5° < \theta < 4.5°$
	Electron detection (HTCC)	$5° < \theta < 35°, 0° < \phi < 360°$
	Efficiency	$\eta > 99\%$
	Neutron detection (FD)	$5° < \theta < 35°$
	Efficiency	$\leq 75\%$
	Neutron detection (CD)	$35° < \theta < 125°$
	Efficiency	10%
	Neutron Detection (BAND)	$155° < \theta < 175°$
	Efficiency	35%
Resolution	Momentum (FD)	$\sigma_p/p = 0.5$–1.5%
	Momentum (CD)	$\sigma_p/p < 5\%$
	Pol. angles (FD)	$\sigma_\theta = 1$–2 mrad
	Pol. angles (CD)	$\sigma_\theta = 2$–5 mrad
	Azim. angles (FD)	$\sigma_\phi < 2$ mrad$/\sin\theta$
	Azim. angles (CD)	$\sigma_\phi = 3$–15 mrad
	Timing (FD)	$\sigma_T = 60$–110 ps
	Timing (CD)	$\sigma_T = 80$–100 ps
	Energy (σ_E/E) (FD)	$0.1/\sqrt{E}$ (GeV)
	Energy (σ_E/E) (FT)	$0.03/\sqrt{E}$ (GeV)
Operation	Luminosity	$L = 10^{35}$ cm^{-2}s^{-1}
DAQ	Data Rate	20 kHz, 800 MB/s., L.T. 95%
Magnetic Field	Solenoid	$B_0 = 5$ T
	Torus	$\int B dl = 0.5$–2.7 Tm at $5° < \theta < 25°$

For the first run period of CLAS12 in the spring and fall of 2018, the luminosity was chosen to not exceed average occupancies of 4% in the R1 drift chambers. The R1 detectors are more exposed to background radiation than R2 and R3. This occupancy limitation typically resulted in beam operations at about 45 nA to 55 nA of beam current, or about 60% to 75% of design luminosity.

10.1.2. Performance of the RICH

Fig. 57 shows the RICH multi-anode photomultiplier array and a single Cherenkov event for a track with the Cherenkov light detected in the MaPMT array. The performance in event reconstruction is illustrated in Fig. 58 for positively charged particles in the design momentum range from 3 to 8 GeV.

10.2. CD reconstruction

Fig. 59 shows selected charged track events in the CVT. The left panels show the projection to the plane perpendicular to the beamline.
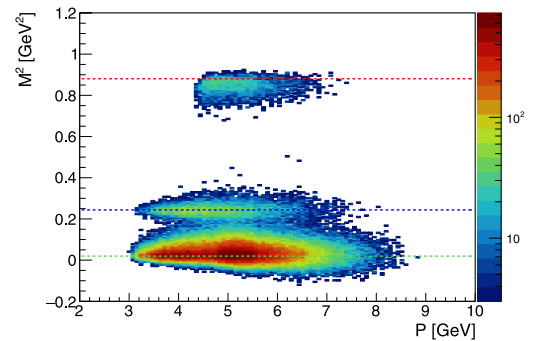

Fig. 58. Charged particle identification in the RICH detector showing the mass squared vs. momentum for positively charged particles. The data show bands for π^+ (bottom), K^+ (middle), and protons (top). The events are from a single aerogel tile, and from photons that hit the MAPMT directly, without reflection from the mirrors. The pion/kaon separation in the RICH sets in where it ranges out with the time-of-flight resolution in the FTOF shown in Fig. 42.

In this view, positively charged particles bend clockwise in the 5 T magnetic field. The innermost 3 double layers mark the SVT and the outer 6 layers indicate the BMT. The panels to the right show the projection onto a plane along the beamline. The CTOF and CND detectors are located radially outward of the CVT and also show the deposited energy where the charged tracks hit. Uncorrelated hits are from neutrals or out-of-time events. Other indicators of the CND performance for charged particles are shown in Fig. 60.

10.2.1. Acceptance and performance of the CD

The Central Detector system covers polar angles from 35° to 125° and the full 360° in azimuth. Fig. 61 shows the acceptance and reconstruction efficiency for charged tracks from simulations with background incorporated according to the beam current. Fig. 62 shows the reconstructed vertex along the beamline (z-axis) for charged particles coming from an empty target cell. The target cell is 5-cm long, and the cell walls are well resolved with an approximate resolution of $\sigma_z < 2$ mm. The final vertex resolution should significantly improve with the optimized detector alignment and calibrations. Events between the cell walls are from beam interactions with the residual cold hydrogen gas in the target cell.

The limited space in the CD makes charged particle identification challenging for momenta $\gtrsim 1$ GeV. The current detector performance in terms of particle identification and tracking resolution is still being optimized and improved. It is expected that the results shown here will continue to improve and the performance will become more in agreement with the expected performance parameters.

The elastic scattering process $ep \to ep$ at relatively low Q^2 can be used to connect the FD where the electron is detected and the CD where most of the elastically scattered protons are detected. The strict
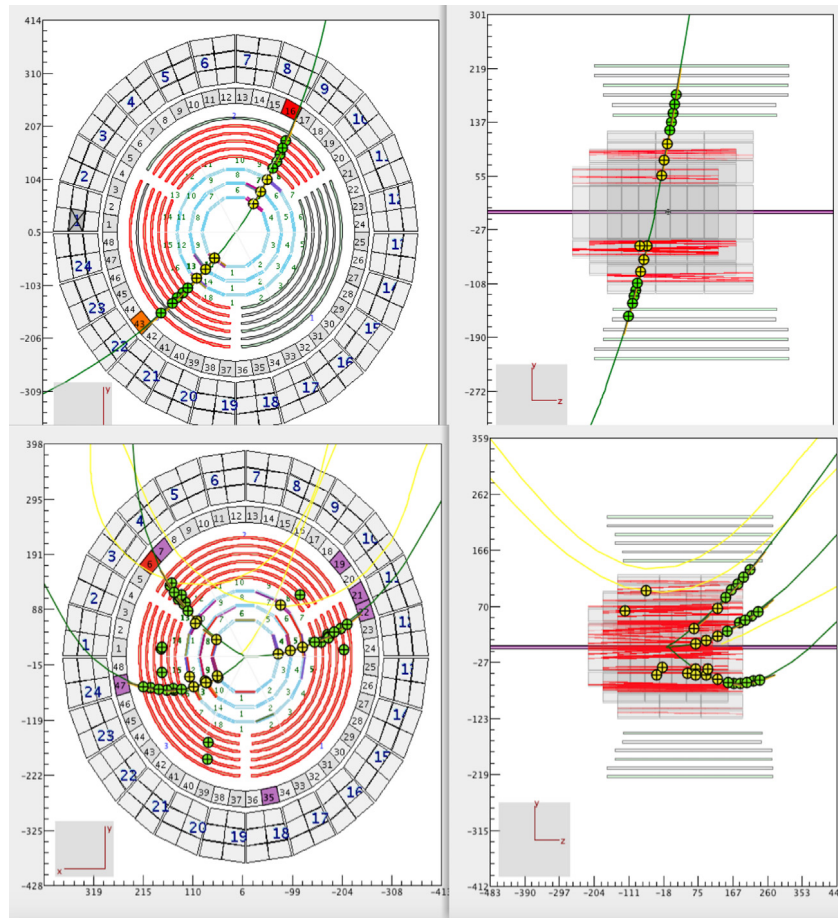
Fig. 59. Top: Example of cosmic ray tracks in the CVT with magnetic field $B = 5$ T. Left: Track projected to the plane perpendicular to the beamline. Right: The same track projected onto a plane along the beamline. Bottom: Multiple track event from beam-target interaction reconstructed in the CLAS12 Central Detector at a beam current of 10 nA. Clockwise bending tracks in the solenoid magnetic field are from positively charged particles.

kinematic correlation in azimuthal angle, given by $\phi_p = \phi_e + 180°$, can be exploited to understand potential relative alignment issues between the FD and CD tracking. Fig. 63 illustrates the correlation in elastic electrons detected in the FD sectors and protons reconstructed in the CD.

10.3. Operating experience

The CLAS12 detector systems were commissioned in the period from December 2017 through February 2018, using beam energies of 2.2, 6.4, and 10.6 GeV. The target cell was filled with liquid hydrogen, except when data were taken on an empty target cell. Data were accumulated with both torus magnet polarities, i.e. electrons bending either toward or away from the beamline, as well as data with different magnetic field strength settings in the torus and solenoid. Understanding of the reconstructed events focused first on the lowest beam energy of 2.2 GeV, for which the elastic peak became quickly visible and could be used to understand the influence of the magnetic field map, the overall detector geometry, and the drift chamber alignment, among other parameters. Fig. 64 shows the elastic electrons detected in each of the six different sectors of the FD to illustrate that quality of the event reconstructions and detector calibrations. After this initial commissioning period, data taking commenced for Run Group A [29], which required use of a liquid-hydrogen target. Use of hydrogen as the target material allowed for the continuation of the commissioning period, while taking production data at the same time. The ability to study exclusive processes plays an essential role in further optimizing the operational performance.

11. Summary

The design criteria, construction details, and operational performance characteristics of the large-acceptance CLAS12 dual-magnet spectrometer in Hall B at Jefferson Laboratory have been described. The spectrometer is now used to study electron-induced reactions at the energy-doubled CEBAF electron accelerator. The spectrometer was commissioned in the period from late 2017 to early 2018, and is now routinely operated in support of a diverse scientific program in the exploration of the internal quark structure of nucleons and nuclei. The major performance criteria, most critically, the operation at instantaneous luminosities up to 10^{35} cm^{-2}s^{-1}, have been met. These criteria are summarized in Table 2. Further improvements in the operational performance of CLAS12 will be realized during the ongoing experimental data analysis and detector optimization studies.
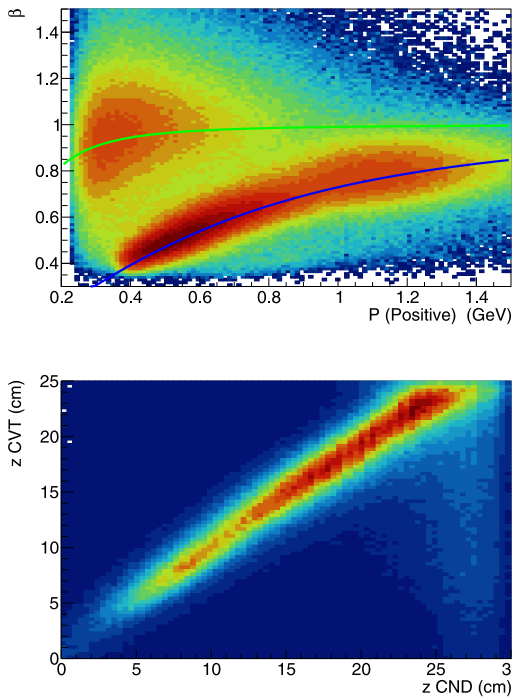
Fig. 60. CND response to charged particles. The upper plot shows β vs. particle momentum for positively charged tracks. The upper green line indicates the nominal relation for pions and the lower blue line indicates the nominal relation for protons. The bottom plot shows the correlation of the hit position of charged tracks measured in the CVT and the hit position measured in the CND using the hit time information. (For interpretation of the references to color in this figure legend, the reader is referred to the web version of this article.)
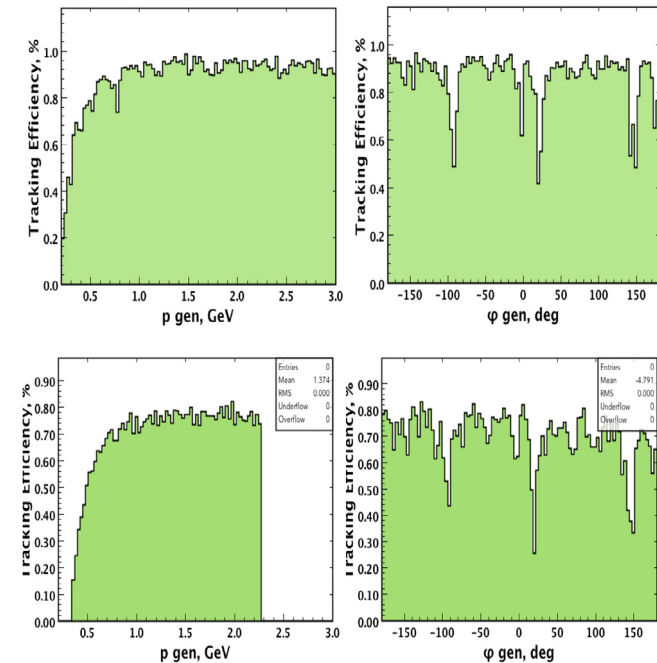

Fig. 61. CVT acceptance and tracking performance. The left panels show the tracking efficiency and acceptances vs. momentum for (top) simulated muon tracks with no beam background and (bottom) the same for protons but with background corresponding to a 50 nA beam current. The right plots show the same quantities vs. azimuthal angle. The 3 ϕ angle dips are due to the support structure separating the 3 BMT segments, and are thus acceptance related. There are also small acceptance gaps between neighboring SVT modules that may account for some acceptance losses as well.
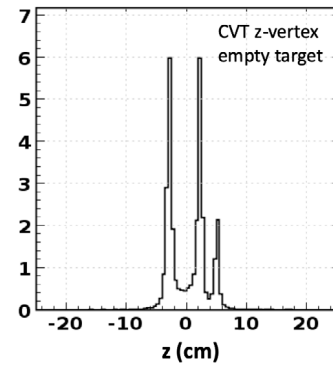

Fig. 62. Reconstructed z-vertices (coordinate along the beamline) for charged tracks in the CD from an empty target cell. The cell walls are clearly visible. The small downstream peak at $z{\sim}5$ cm is from events originating in a thin thermal shielding foil.
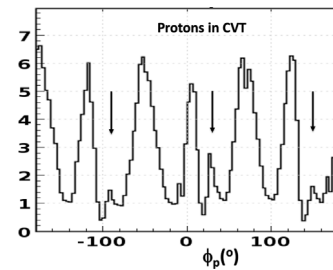

Fig. 63. Elastically scattered protons reconstructed in the CVT and CTOF. The proton peaks show the reflection of the 6 FD sectors where the electrons are detected. In addition there is a 3-fold modulation (seen in the different widths of 3 of the peaks) due to the 3 BMT sectors where protons are detected. The arrows indicate the physical position of the support structures at the boundaries between two BMT segments. The azimuthal angle is the reconstructed angle at the production target. Due to the clockwise curvature of proton tracks in the solenoid magnetic field (see bottom plot in Fig. 59) the support structures appear shifted by a certain $\Delta\phi_p$ amount relative to their locations in the lab. (The vertical axes is in arbitrary units).
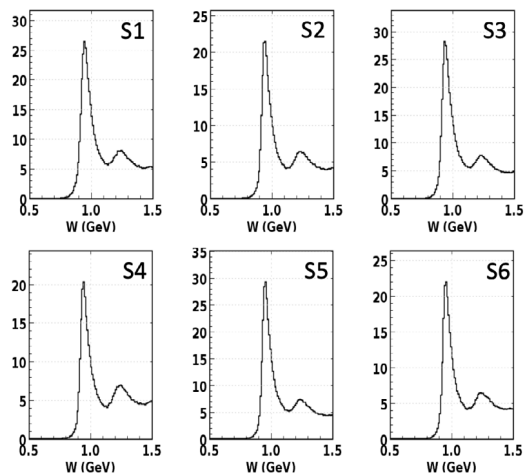

Fig. 64. Elastically scattered electrons off protons from 2.2 GeV data in all of the FD sectors showing the reconstructed W distributions.

References

[1] R.W. McAllister, R. Hofstadter, Elastic scattering of 188-MeV electrons from the proton and the α particle, Phys. Rev. 102 (1956) 851, http://dx.doi.org/10.1103/PhysRev.102.851.

[2] M. Breidenbach, et al., Observed behavior of highly inelastic electron-proton scattering, Phys. Rev. Lett. 23 (1969) 935, http://dx.doi.org/10.1103/PhysRevLett.23.935.

[3] S.E. Kuhn, J.-P. Chen, E. Leader, Spin structure of the nucleon - status and recent results, Prog. Part. Nucl. Phys. 63 (2009) 1, http://dx.doi.org/10.1016/j.ppnp.2009.02.001.

[4] C.W. Leemann, D.R. Douglas, G.A. Krafft, The continuous electron beam accelerator facility: CEBAF at the Jefferson laboratory, Ann. Rev. Nucl. Part. Sci. 51 (2001) 413, http://dx.doi.org/10.1146/annurev.nucl.51.101701.132327.

[5] B.A. Mecking, et al., The CEBAF large acceptance spectrometer (CLAS), Nucl. Instrum. Methods A 503 (2003) http://dx.doi.org/10.1016/S0168-9002(03)01001-5.

[6] V.D. Burkert, Jefferson lab at 12 GeV: The science program, Ann. Rev. Nucl. Part. Sci. 68 (2018) 405, http://dx.doi.org/10.1146/annurev-nucl-101917-021129.

[7] R. Fair, et al., The CLAS12 superconducting magnets, Nucl. Instrum. Methods A (2020) http://dx.doi.org/10.1016/j.nima.2020.163578, in press (see this issue).

[8] M.D. Mestayer, et al., The CLAS12 drift chamber system, Nucl. Instrum. Methods A 959 (2020) 163518, http://dx.doi.org/10.1016/j.nima.2020.163518.

[9] Y.G. Sharabian, et al., The CLAS12 high threshold Cherenkov counter, Nucl. Instrum. Methods A (2020) in press (see this issue).

[10] G. Adams, et al., The CLAS Cherenkov detector, Nucl. Instrum. Methods A 465 (2001) 414, http://dx.doi.org/10.1016/S0168-9002(00)01313-9.

[11] M. Ungaro, et al., The CLAS12 low threshold Cherenkov counter, Nucl. Instrum. Methods A (2020) http://dx.doi.org/10.1016/j.nima.2020.163420, in press (see this issue).

[12] M. Contalbrigo, et al., The CLAS12 ring imaging Cherenkov detector, Nucl. Instrum. Methods A (2020) in press (see this issue).

[13] D.S. Carman, et al., The CLAS12 forward time-of-flight system, Nucl. Instrum. Methods A (2020) http://dx.doi.org/10.1016/j.nima.2020.163629, in press (see this issue).

[14] M. Amarian, et al., The CLAS forward electromagnetic calorimeter, Nucl. Instrum. Methods A 460 (2001) 239, http://dx.doi.org/10.1016/S0168-9002(00)00996-7.

[15] G. Asryan, et al., The CLAS12 forward electromagnetic calorimeter, Nucl. Instrum. Methods A 959 (2020) 163425, http://dx.doi.org/10.1016/j.nima.2020.163425.

[16] A. Acker, et al., The CLAS12 forward tagger, Nucl. Instrum. Methods A 959 (2020) 163475, http://dx.doi.org/10.1016/j.nima.2020.163475.

[17] M.A. Antonioli, et al., The CLAS12 silicon vertex tracker, Nucl. Instrum. Methods A (2020) in press (see this issue).

[18] F. Bossu, et al., The CLAS12 micromegas vertex tracker, Nucl. Instrum. Methods A (2020) in press (see this issue).

[19] V. Baturin, et al., Dynamic magnetic shield for the CLAS12 central TOF detector photomultiplier tubes, Nucl. Instrum. Methods A 664 (2012) 11, http://dx.doi.org/10.1016/j.nima.2011.10.003.

[20] D.S. Carman, et al., The CLAS12 central time-of-flight system, Nucl. Instrum. Methods A (2020) http://dx.doi.org/10.1016/j.nima.2020.163626, in press (see this issue).

[21] P. Chatagnon, et al., The CLAS12 central neutron detector, Nucl. Instrum. Methods A 959 (2020) 163441, http://dx.doi.org/10.1016/j.nima.2020.163441.

[22] The CLAS12 Back Angle Neutron Detector (BAND), Nucl. Instrum. Methods in preparation.

[23] N. Baltzell, et al., The CLAS12 beamline and its performance, Nucl. Instrum. Methods A 959 (2020) 163421, http://dx.doi.org/10.1016/j.nima.2020.163421.

[24] M. Ungaro, et al., The CLAS12 Geant4 simulation, Nucl. Instrum. Methods A 959 (2020) 163422, http://dx.doi.org/10.1016/j.nima.2020.163422.

[25] S. Boyarinov, et al., The CLAS12 data acquisition system, Nucl. Instrum. Methods A (2020) in press (see this issue).

[26] B. Raydo, et al., The CLAS12 trigger system, Nucl. Instrum. Methods A (2020) http://dx.doi.org/10.1016/j.nima.2020.163529, in press (see this issue).

[27] V. Ziegler, et al., The CLAS12 software framework and event reconstruction, Nucl. Instrum. Methods A 959 (2020) 163472, http://dx.doi.org/10.1016/j.nima.2020.163472.

[28] V. Burkert, S. Stepanyan, J.A. Tan, M. Ungaro, CLAS12 note 2017-018, 2017, https://misportal.jlab.org/mis/physics/clas12/viewFile.cfm/2017-018pdf?documentId=54.

[29] CLAS12 Run Groups, https://www.jlab.org/Hall-B/clas12-web/Hall_B_experiment_run_groups.pdf.